Systematic analysis of inelastic α scattering off self-conjugate A=4n nuclei

AUTHOR(S):

Adachi, S.; Kawabata, T.; Minomo, K.; Kadoya, T.; Yokota, N.; Akimune, H.; Baba, T.; ... Uesaka, T.; Yoshida, H. P.; Yoshida, S.

CITATION:

Adachi, S. ...[et al]. Systematic analysis of inelastic α scattering off self-conjugate A=4n nuclei. Physical Review C 2018, 97(1): 014601.

ISSUE DATE:

2018-01

URL:

http://hdl.handle.net/2433/230325

Systematic analysis of inelastic α scattering off self-conjugate $A = 4n$ nuclei

S. Adachi,[1,*] T. Kawabata,[1] K. Minomo,[2] T. Kadoya,[1] N. Yokota,[1] H. Akimune,[3] T. Baba,[1] H. Fujimura,[4] M. Fujiwara,[2,5] Y. Funaki,[6] T. Furuno,[1] T. Hashimoto,[1] K. Hatanaka,[2] K. Inaba,[1] Y. Ishii,[1] M. Itoh,[7] C. Iwamoto,[2,†] K. Kawase,[2,‡] Y. Maeda,[8] H. Matsubara,[9] Y. Matsuda,[7] H. Matsuno,[10,§] T. Morimoto,[10] H. Morita,[10,§] M. Murata,[1] T. Nanamura,[10,§] I. Ou,[11] S. Sakaguchi,[12] Y. Sasamoto,[13] R. Sawada,[10,‖] Y. Shimizu,[14] K. Suda,[14] A. Tamii,[2] Y. Tameshige,[15] M. Tsumura,[1] M. Uchida,[16] T. Uesaka,[14] H. P. Yoshida,[2] and S. Yoshida[10,¶]

[1]*Department of Physics, Kyoto University, Kitashirakawa-Oiwake, Sakyo, Kyoto 606-8502, Japan*
[2]*Research Center for Nuclear Physics (RCNP), Osaka University, Ibaraki, Osaka 567-0047, Japan*
[3]*Department of Physics, Konan University, Higashinada, Kobe, Hyogo 658-8501, Japan*
[4]*Department of Physics, Wakayama Medical University, Kimiidera, Wakayama 640-0011, Japan*
[5]*National Institutes for Quantum and Radiological Science and Technology, Tokai, Ibaraki 319-1195, Japan*
[6]*College of Science and Engineering, Kanto Gakuin University, Kanazawa, Yokohama, Kanagawa 236-8501, Japan*
[7]*Cyclotron and Radioisotope Center (CYRIC), Tohoku University, Sendai, Miyagi 980-8578, Japan*
[8]*Faculty of Engineering, University of Miyazaki, Gaukuen-Kibanadai, Miyazaki 889-2192, Japan*
[9]*School of Medicine, Tokyo Women's Medical University, Kawada, Shinjuku, Tokyo 162-8666, Japan*
[10]*Faculty of Science, Kyoto University, Kitashirakawa-Oiwake, Sakyo, Kyoto 606-8502, Japan*
[11]*Department of Physics, Okayama University, Tsushimanaka, Kita, Okayama 700-8530, Japan*
[12]*Department of Physics, Kyushu University, Moto-oka, Nishi, Fukuoka 819-0395, Japan*
[13]*Center for Nuclear Study (CNS), The University of Tokyo, Hongo, Bunkyo, Tokyo 113-0033, Japan*
[14]*RIKEN Nishina Center for Accelerator-Based Science, Hirosawa, Wako, Saitama 351-0198, Japan*
[15]*Proton Therapy Center, Fukui Prefectural Hospital, Yotsui, Fukui 910-0846, Japan*
[16]*School of Science, Tokyo Institute of Technology, Ookayama, Meguro, Tokyo 152-8550, Japan*

(Received 16 October 2017; published 3 January 2018)

We systematically measured the differential cross sections of inelastic α scattering off self-conjugate $A = 4n$ nuclei at two incident energies $E_\alpha = 130$ MeV and 386 MeV at Research Center for Nuclear Physics, Osaka University. The measured cross sections were analyzed by the distorted-wave Born-approximation (DWBA) calculation using the single-folding potentials, which are obtained by folding macroscopic transition densities with the phenomenological αN interaction. The DWBA calculation with the density-dependent αN interaction systematically overestimates the cross sections for the $\Delta L = 0$ transitions. However, the DWBA calculation using the density-independent αN interaction reasonably well describes all the transitions with $\Delta L = 0$–4. We examined uncertainties in the present DWBA calculation stemming from the macroscopic transition densities, distorting potentials, phenomenological αN interaction, and coupled channel effects in ^{12}C. It was found that the DWBA calculation is not sensitive to details of the transition densities nor the distorting potentials, and the phenomenological density-independent αN interaction gives reasonable results. The coupled-channel effects are negligibly small for the 2^+_1 and 3^-_1 states in ^{12}C, but not for the 0^+_2 state. However, the DWBA calculation using the density-independent interaction at $E_\alpha = 386$ MeV is still reasonable even for the 0^+_2 state. We concluded that the macroscopic DWBA calculations using the density-independent interaction are reliably applicable to the analysis of inelastic α scattering at $E_\alpha \sim 100$ MeV/u.

DOI: 10.1103/PhysRevC.97.014601

I. INTRODUCTION

Inelastic α scattering is one of useful probes to examine nuclear structure because its reaction mechanism is relatively simple. Since both spin and isospin of the α particle are zero, inelastic α scattering has selectivity to isoscalar natural-parity transitions where transferred spin and isospin are $\Delta S = 0$

*sadachi@rcnp.osaka-u.ac.jp; Present address: Research Center for Nuclear Physics (RCNP), Osaka University, Ibaraki, Osaka 567-0047, Japan.
†Present address: Center for Nuclear Study (CNS), The University of Tokyo, Hongo, Bunkyo, Tokyo 113-0033, Japan.
‡Present address: Hiroshima Synchrotron Radiation Center, Hiroshima University, Higashi Hiroshima, 739-0046, Japan.
§Present address: Department of Physics, Kyoto University, Kitashirakawa-Oiwake, Sakyo, Kyoto 606-8502, Japan.
‖Present address: Department of Astronomy, Kyoto University, Kitashirakawa-Oiwake, Sakyo, Kyoto 606-8502, Japan.
¶Present address: Department of Physics, The University of Tokyo, Hongo, Bunkyo, Tokyo 113-0033, Japan.

and $\Delta T = 0$. The cross sections are reasonably reproduced by means of a simple folding-model calculation, and are approximately proportional to the square of the relevant transition matrix elements. Angular distributions of cross sections are characterized by the transferred angular-momentum ΔL, but are not sensitive to details of nuclear wave functions. Therefore, the multipole decomposition analysis (MDA), in which measured cross sections are fitted by calculated cross sections for various multipole transitions, works well to obtain strength distributions of isoscalar natural-parity excitations.

Isoscalar giant monopole resonances (ISGMRs) and isoscalar giant dipole resonances (ISGDR) are extensively examined by the MDA for the inelastic α scattering [1–10]. The ISGMR and ISGDR strength distributions were successfully extracted from continuous excitation-energy spectra by the MDA. These analyses gave the nuclear incompressibility of the symmetric nuclear matter [3,6,8]. Recently, inelastic α scattering off unstable nuclei becomes feasible [11,12] because ISGMRs in unstable nuclei are of special interest in nuclear physics to examine the nuclear incompressibility of the asymmetric nuclear matter.

Inelastic α scattering is also useful from the viewpoint of nuclear cluster physics. For example, the missing 2_2^+ state in ^{12}C was found by the MDA of the ^{12}C(α,α') reaction at $E_\alpha = 386$ MeV for the first time [13]. This 2_2^+ state was incontrovertibly predicted by the 3α cluster model as an excited state of the 0_2^+ state (the Hoyle state) [14–16], but no experimental attempt to search for this state had been successful for a long time [17–19].

It is pointed out that large isoscalar monopole transition strengths are a signature of cluster excitation in atomic nuclei [20]. This is theoretically explained by using the Bayman-Bohr theorem [21] in Ref. [22]. The cluster degrees of freedom are inherently conserved even in case simple shell-model wave functions, and can be activated by the monopole excitation. As an example, the Hoyle state, which has a spatially developed 3α cluster structure, is excited with a large isoscalar monopole strength of $B(E0; IS) = 121 \pm 9$ fm^4 [20,23]. This strength is about three times greater than the single-particle limit of the isoscalar monopole strength in ^{12}C [24]. For ^{24}Mg, several 0^+ states are strongly excited by isoscalar monopole transitions in inelastic α scattering as reported in Ref. [25]. The theoretical calculation suggests these 0^+ states have spatially developed cluster structures [26]. Inelastic α scattering is the best probe to measure the isoscalar monopole transition strengths, and it is, therefore, suitable to search for cluster states.

As described above, measurements of isoscalar natural-parity transition strengths by means of inelastic α scattering are widely performed [1–10,13,25,27–29], assuming the linear proportional relation between the cross sections and the square of the transition matrix elements. However, a contradictory result to the linear proportional relation was reported in the monopole excitation to the Hoyle state from the ground state in ^{12}C. The isoscalar monopole strength determined from the inelastic electron scattering exhausts about 15% of the energy-weighted sum-rule (EWSR) strength [24,30], but that from the inelastic α scattering exhausts as small as 7.6% [27]. This discrepancy is called the missing monopole strength of the Hoyle state.

In Ref. [31], the authors performed a full microscopic folding-model analysis of the inelastic $\alpha + {}^{12}$C scattering at the intermediate energies using a complex density-dependent interaction and the reliable wave functions of the ground and Hoyle states in ^{12}C from the 3α resonating group method (RGM) calculation [16]. The monopole excitation strength predicted by the 3α RGM calculation is very close to the strength reported from the inelastic electron scattering. Nevertheless, the calculated cross sections of the inelastic α scattering for the Hoyle state using the 3α RGM wave function were significantly larger than the measured cross sections. This discrepancy was consistent with the previous results [27] that the excitation strength for the Hoyle state determined by inelastic α scattering was much smaller than that determined by inelastic electron scattering.

The authors of Ref. [31] claimed that this problem is due to the weakly bound structure of the Hoyle state, which significantly enhances the absorption in the exit $\alpha + {}^{12}\mathrm{C}^*(0_2^+)$ channel, and the reaction mechanism of inelastic α scattering might strongly couple to the nuclear structure. Therefore, the approximate linear proportional relation between cross sections and relevant transition strengths might not be used in the analysis of inelastic alpha scattering. It leads us to a serious situation in which we cannot reliably examine nuclear structure by means of inelastic α scattering.

In the present work, we systematically measured the cross sections of inelastic α scattering at $E_\alpha = 130$ and 386 MeV, exciting low-lying states in ^{12}C, ^{16}O, ^{20}Ne, ^{24}Mg, ^{28}Si, and ^{40}Ca. The measured cross sections were compared with the distorted-wave Born-approximation (DWBA) calculations using the known values of the electromagnetic transition strengths in order to examine the applicability of these calculations for the experimental data. We also studied uncertainties of the DWBA calculations from the distorting potentials, phenomenological interaction, transition densities, and coupled-channel effects.

II. EXPERIMENT

A. Experimental setups and measurements

A series of the measurements was performed at Research Center of Nuclear Physics (RCNP), Osaka University. A 130-MeV ^{4}He^{2+} beam provided by the AVF cyclotron was achromatically transported to the target. On the other hand, a 386-MeV ^{4}He^{2+} beam was extracted from the ring cyclotron after the preacceleration by the AVF cyclotron. The 386-MeV ^{4}He^{2+} beam was dispersively transported to the target in order to improve the excitation-energy resolution in the measurements with the solid targets except the ^{20}Ne gas target. The dispersive beam transport for the ^{20}Ne gas target could not be done because the energy spread of the ^{4}He^{2+} beam from the ring cyclotron ($\Delta E = 250$ keV) was wider than the usual ($\Delta E = 100$ keV) when the ^{20}Ne gas target was used. The dispersive transport of such a beam with a wide energy spread results in unacceptably large beam size on the target.

Table I summarizes the target nuclei, thicknesses, and isotope enrichment. The SiO_2 foil was used as the ^{16}O target. The contribution from ^{nat}Si was subtracted using a ^{nat}Si target. For the ^{20}Ne target, a cooling gas target system was used

TABLE I. Thicknesses and isotope enrichment of the targets used in the present measurements with the $^4He^{2+}$ beams at $E_\alpha = 130$ and 386 MeV. All the foil targets are self-supporting.

Nucleus	State	Thickness	Enrichment	$^4He^{2+}$ energy	
				130	386
		(mg/cm^2)	(%)	(MeV)	
^{12}C	foil	2.2	98.9[a]	✓	✓
SiO_2[b]	foil	2.2	99.8[c]	✓	✓
^{20}Ne	gas[d]	2.4	99.95		✓
^{24}Mg	foil	1.2	99.92	✓	
^{24}Mg	foil	2.5	>99.9		✓
^{28}Si	foil	1.72	92.2[a]	✓	
^{28}Si	foil	2.16	92.2[a]		✓
^{40}Ca	foil	1.63	>99.9	✓	✓

[a]Natural abundance.
[b]The SiO_2 foil was used as the ^{16}O target.
[c]Natural abundance of ^{16}O.
[d]See the text for more details

[32,33]. The isotopically enriched ^{20}Ne gas with a purity of 99.95% was filled into the gas cell and cooled by liquid N_2 in order to increase the target density. The entrance and exit windows were sealed with aramid films with a thickness of 4 μm. The pressure and temperature of the ^{20}Ne gas were monitored using the diaphragm pressure gauge and the platinum resistance thermometer during the measurements. The gas pressure and temperature were 78.0 ± 1.2 kPa and 86.5 ± 0.4 K, respectively. The effective thickness of the ^{20}Ne gas target along the beam axis was calibrated by filling the gas cell with the CO_2 gas at the pressure close to that of the ^{20}Ne gas. We determined the thickness of the ^{20}Ne gas as 11.2 ± 1.7 mm by comparing the measured cross section of the elastic α scattering from ^{12}C with the known value. This thickness corresponds to 2.4 ± 0.4 mg/cm^2.

Scattered α particles were analyzed using the magnetic spectrometer Grand Raiden (GR) [34]. Figure 1(a) shows an overview of GR and its related instruments. The two multiwire drift chambers (MWDC1 and 2) and two plastic scintillation counters (PS1 and 2) were installed at the focal plane of GR. The MWDCs were used to determine the trajectories of scattered particles at the focal plane. The data-acquisition trigger was made when both the plastic scintillation counters generated signals in coincidence.

Beam currents during the measurements were monitored using the four different Faraday cups. The zero-degree Faraday cup (0 deg. FC), which was located at the downstream of the focal plane, was used for the measurements at $\theta_{lab} = 0^\circ$, and the primary beam was transported to the 0 deg. FC through GR. When the 0 deg. FC was used, the low-lying excited states at $E_x < 2.5$ MeV for $E_\alpha = 130$ MeV and at $E_x < 7.5$ MeV for $E_\alpha = 386$ MeV cannot be measured due to the geometrical limitation of the MWDCs. The lateral distances between trajectories of the primary beam and scattered α particles exciting such low-lying states at the focal plane were too short for the MWDCs to detect the scattered α particles separately from the primary beam. To measure the (α,α') spectra for such low-lying states at $\theta_{lab} = 0^\circ$, an alternative Faraday cup called the focal plane Faraday cup (FP-FC) was used. The FP-FC was installed at the front of the MWDCs as shown in Fig. 1(b). Since the FP-FC was placed very close to the sensitive area of the MWDCs, the FP-FC enabled us to detect the scattered α particles exciting the low-lying states by the MWDCs. However, huge background γ rays from the FP-FC hit both the MWDCs and the trigger plastic scintillators, therefore the beam intensity was limited lower than 1.0 nA when the FP-FC was used.

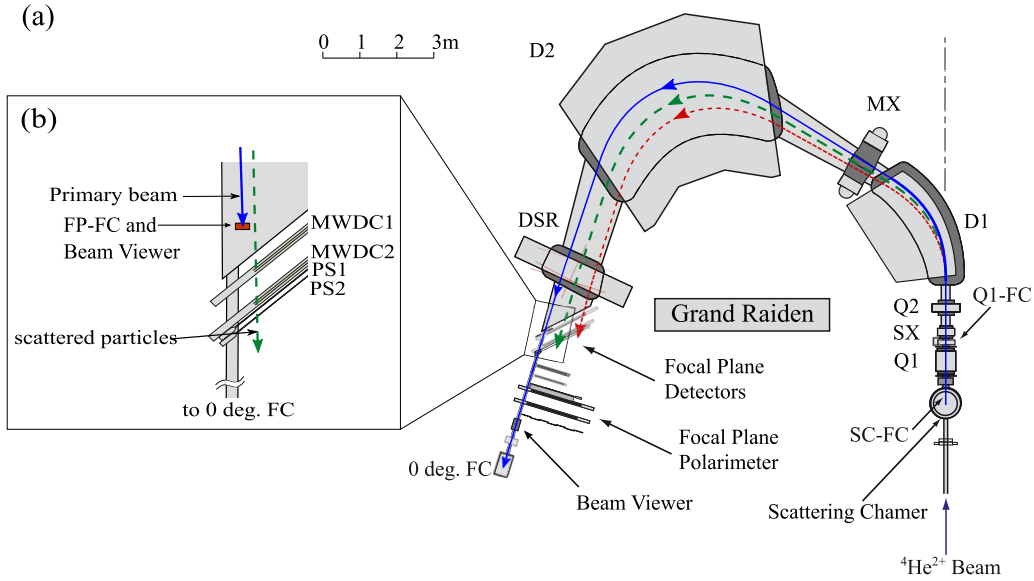

FIG. 1. (a) An overview of the Grand Raiden spectrometer and its related instruments. The experimental setup at $\theta_{lab} = 0^\circ$ is shown [35]. The solid lines with arrow heads in the spectrometer show the trajectories of primary beam particles, and dashed and dotted lines show those of scattered α particles. The primary beam is guided to the Faraday cup, which is located at the downstream of the spectrometer (0 deg. FC). (b) A schematic view around the focal plane. In case of the spectrum measurements for low-lying excited states, the primary beam is stopped at the focal plane Faraday cup (FP-FC), which is placed at the upstream of the focal plane.

TABLE II. Angular ranges for the cross-section measurements of elastic α scattering at $E_\alpha = 130$ and 386 MeV.

Nucleus	Elastic scattering	
	$E_\alpha = 130$ MeV θ_{cm} (deg)	$E_\alpha = 386$ MeV θ_{cm} (deg)
^{12}C	4.97°–70.3°	2.73°–34.2°
^{16}O	4.65°–58.1°	2.45°–28.5°[a]
^{20}Ne	Not measured	5.11°–27.4°
^{24}Mg	5.39°–70.4°	5.26°–28.8°[b]
^{28}Si	8.03°–48.8°	Not measured
^{40}Ca	4.08°–59.3°	Not measured

[a]Ref. [29].
[b]Ref. [25].

For the measurements at $\theta_{lab} = 2.5°$–$5.0°$, the primary beam was stopped at the Faraday cup behind the Q1 magnet of GR (Q1-FC) as shown in Fig. 1(a). The Faraday cup installed in the scattering chamber (SC-FC) was used in the measurements at the backward angles $\theta_{lab} \geqslant 6.0°$. Charge collection efficiencies of the four Faraday cups were calibrated within the 3% uncertainties by using a beam monitor consisting of plastic scintillators located on the beam line.

Table II summarizes the angular ranges for the cross-section measurements of elastic α scattering at $E_\alpha = 130$ and 386 MeV, respectively. The cross sections at $E_\alpha = 130$ MeV were measured for all the targets except ^{20}Ne. The cross sections at backward angles between $\theta_{cm} = 41.9°$ and 70.3° were measured using different experimental setups with the Si and CsI(Tl) detectors. The cross sections at $E_\alpha = 386$ MeV were measured for ^{12}C and ^{20}Ne only, although the cross sections for ^{24}Mg and ^{16}O were taken from Refs. [25] and [29], respectively. Since the cross sections for ^{28}Si and ^{40}Ca at $E_\alpha = 386$ MeV were not measured in the present experiment nor taken from previous works, a special treatment was done in the analysis of ^{28}Si and ^{40}Ca as described in Sec. III A.

B. Data reduction and cross sections

Scattered α particles were well separated from background protons and deuterons using the time of flight from the target to the focal plane of GR. Beam particles passing through the target spread out due to multiple Coulomb scattering and hit beam ducts. These particles caused continuous background in excitation-energy spectra at forward angles. These background events were removed using the vertical position information of scattered particles at the focal plane because α particles scattered from the target were vertically focused near the focal plane whereas background particles scattered at different positions were not focused [5]. Scattering angles within the angular acceptance of the GR spectrometer were calibrated using the sieve slit as reported in Ref. [35]. The excitation energies were calibrated using the peak position for the known excited states in the measured spectra.

An (α,α') spectrum measured using the ^{20}Ne gas target is shown in Fig. 2(a). Several discrete peaks for the ground and excited states in ^{12}C, ^{14}N, ^{16}O, and ^{35}Cl were observed.

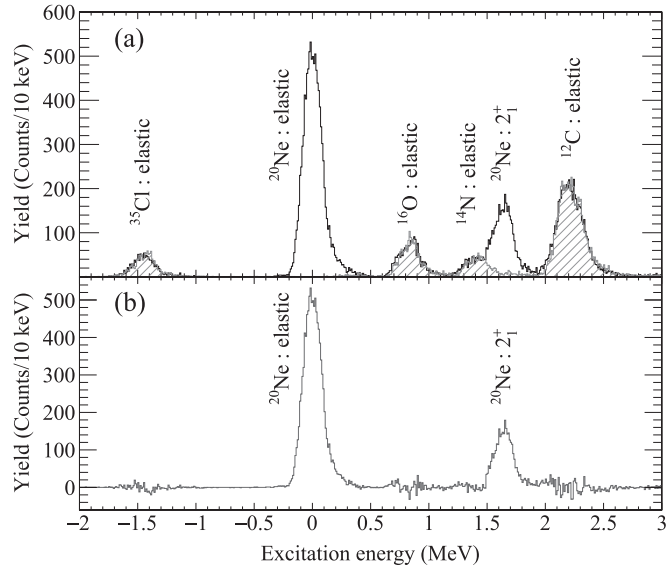

FIG. 2. Excitation-energy spectra for the ^{20}Ne(α,α') reaction at $E_\alpha = 386$ MeV measured at $\theta_{lab} = 10.8°$. (a) The open histogram represents the excitation-energy spectrum obtained using the gas cell filled with ^{20}Ne. The hatched histogram represents the normalized spectrum obtained using the empty gas cell. (b) A background-free ^{20}Ne(α,α') spectrum obtained by subtracting the background events originated from aramid films.

These nuclei are contained in the aramid films at the entrance and exit windows of the gas cell. In order to subtract the background events due to the aramid windows, the background measurements with the empty gas cell was carried out. The pressure of the empty gas cell was kept at the order of 10^{-2} Pa. The measured background spectrum is shown by the hatched histogram in Fig. 2(a). The background-free spectra were successfully obtained by subtracting background spectra as seen in Fig. 2(b). The normalization factor for the background subtraction was calculated by taking into account the beam intensities, target thicknesses, and detector efficiencies. Similarly, the background-free excitation energy spectra for ^{16}O were obtained by subtracting the excitation energy spectra for ^{nat}Si from those for $^{nat}SiO_2$.

The obtained excitation-energy spectra for the (α,α') reactions at $E_\alpha = 130$ MeV at $\theta_{lab} = 0.0°$ are shown in Fig. 3. The typical energy resolution of the (α,α') spectrum at $E_\alpha = 130$ MeV and 386 MeV was about 85 keV and 95 keV at the full width at half maximum (FWHM) for the solid targets except ^{20}Ne, respectively. On the other hand, the energy resolution of the ^{20}Ne(α,α') reaction at $E_\alpha = 386$ MeV was about 250 keV at FWHM.

Finally, the angular distributions of the (α,α') cross sections at $E_\alpha = 130$ and 386 MeV were obtained. The measured excited states are listed in Table III.

The measured cross sections of the elastic α scattering relative to the Rutherford cross sections (Rutherford ratio) are presented in Figs. 4 and 5. Similarly, the measured (α,α') cross sections for the $\Delta L = 0$, $\Delta L = 2$, and $\Delta L = 3$ transitions at $E_\alpha = 386$ and 130 MeV are shown in Figs. 6 and 7, Figs. 8

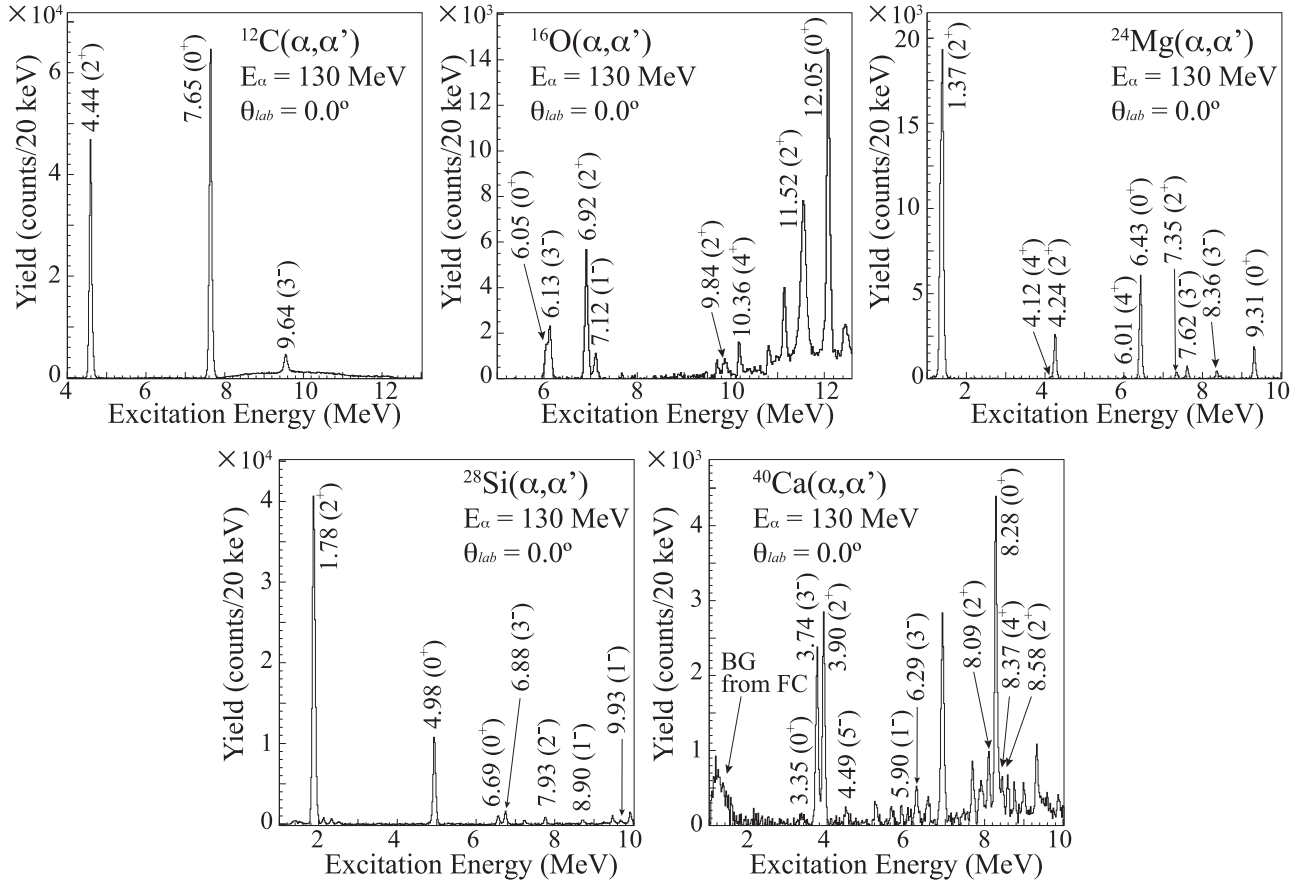

FIG. 3. Excitation-energy spectra for the (α,α′) reactions at $E_\alpha = 130$ MeV measured at $\theta_{\rm lab} = 0.0°$.

and 9, and Figs. 10 and 11, respectively. Figures 12 and 13 show those for $\Delta L = 4$ and $\Delta L = 1$, respectively. In Figs. 7–13, we show only the cross sections to the excited states whose electromagnetic excitation strengths from the ground states were reported in the previous studies [24,36–38].

III. DISTORTED-WAVE BORN-APPROXIMATION CALCULATION

We performed the DWBA calculations using the computer code ECIS-95 [39] in order to compare the measured cross sections with the calculations. The optical-model potentials for

TABLE III. Listing of the excited states analyzed in the present work. Note that the 0^+, 1^-, 2^+, 3^-, and 4^+ states are discussed in this paper.

Nucleus	J^π	E_x (MeV)	E_α 130 (MeV)	E_α 386 (MeV)	Nucleus	J^π	E_x (MeV)	E_α 130 (MeV)	E_α 386 (MeV)	Nucleus	J^π	E_x (MeV)	E_α 130 (MeV)	E_α 386 (MeV)	Nucleus	J^π	E_x (MeV)	E_α 130 (MeV)	E_α 386 (MeV)
^{12}C	0^+_1	0.00	✓	✓	^{16}O	0^+_3	12.05	✓	✓	^{24}Mg	2^+_3	7.35	✓	✓[b]	^{28}Si	1^-_1	8.90	✓	
^{12}C	2^+_1	4.44	✓	✓	^{20}Ne	0^+_1	0.00		✓	^{24}Mg	3^-_1	7.62	✓	✓[b]	^{28}Si	2^+_4	9.48	✓	
^{12}C	0^+_2	7.65	✓	✓	^{20}Ne	2^+_1	1.67		✓	^{24}Mg	3^-_2	8.36	✓	✓[b]	^{40}Ca	0^+_1	0.00	✓	
^{12}C	3^-_1	9.64	✓	✓	^{20}Ne	4^+_1	4.25		✓	^{24}Mg	2^+_5	9.00	✓	✓[b]	^{40}Ca	0^+_2	3.35	✓	
^{16}O	0^+_1	0.00	✓	✓[a]	^{20}Ne	3^-_1	5.62		✓	^{24}Mg	2^+_7	10.36	✓		^{40}Ca	3^-_1	3.74	✓	✓
^{16}O	0^+_2	6.05	✓		^{20}Ne	0^+_2	6.73		✓	^{28}Si	0^+_1	0.00	✓		^{40}Ca	2^+_1	3.90	✓	✓
^{16}O	3^-_1	6.13	✓	✓	^{24}Mg	0^+_1	0.00	✓	✓[b]	^{28}Si	2^+_1	1.78	✓	✓	^{40}Ca	1^-_1	5.90	✓	
^{16}O	2^+_1	6.92	✓	✓	^{24}Mg	2^+_1	1.37	✓	✓[b]	^{28}Si	4^+_1	4.62	✓		^{40}Ca	3^-_2	6.29	✓	
^{16}O	1^-_1	7.12	✓		^{24}Mg	4^+_1	4.12	✓		^{28}Si	0^+_2	4.98	✓	✓	^{40}Ca	2^+_2	8.09	✓	
^{16}O	2^+_2	9.84	✓		^{24}Mg	2^+_2	4.24	✓		^{28}Si	3^-_1	6.88	✓		^{40}Ca	2^+_3	8.58	✓	
^{16}O	4^+_1	10.36	✓		^{24}Mg	4^+_2	6.01	✓		^{28}Si	2^+_2	7.93	✓						
^{16}O	2^+_3	11.52	✓	✓	^{24}Mg	0^+_2	6.43	✓	✓[b]	^{28}Si	2^+_3	8.26	✓						

[a]Ref. [29].
[b]Ref. [25].

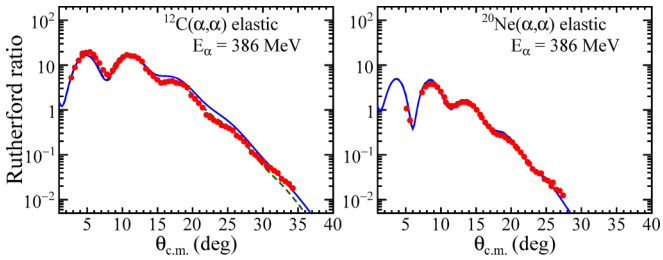

FIG. 4. Measured cross sections of elastic α scattering off ^{12}C and ^{20}Ne at $E_\alpha = 386$ MeV relative to the Rutherford cross sections (Rutherford ratio) compared with the theoretical calculation. The solid circles with error bars show the measured cross sections. The solid and dashed lines represent the results of calculation with the density-independent (DI) and density-dependent (DD) αN interactions, respectively. For the detailed discussion on the theoretical calculations, see Sec. III.

the elastic α scattering were used as the distorting potentials in the DWBA calculation. The same distorting potential was used in the entrance and exit channels for each nucleus. The optical-model potentials and the transition potentials between the ground and excited states were calculated using the single-folding model.

A. Optical-model potential for the elastic α scattering and the effective αN interaction

An optical-model potential $U(r)$ for elastic α scattering is obtained by folding the ground-state density distribution of the target nucleus with αN interactions as follows:

$$U(r) = \int d\boldsymbol{r}'\,\rho_0(r')\,u[|\boldsymbol{r}-\boldsymbol{r}'|,\rho_0(r')], \qquad (1)$$

where $\boldsymbol{r}'$ and $\boldsymbol{r}$ denote the position of a pointlike nucleon in the target and an incident α particle, respectively. $\rho_0(r')$ is the ground-state density distribution of a target nucleus. $u[|\boldsymbol{r}-\boldsymbol{r}'|,\rho_0(r')]$ is the phenomenological αN interaction parameterized by five adjustable parameters [40] as

$$u[|\boldsymbol{r}-\boldsymbol{r}'|,\rho_0(r')] = -v\left[1+\beta\rho_0^{2/3}(r')\right]e^{-|\boldsymbol{r}-\boldsymbol{r}'|^2/\alpha_v^2} - iw\left[1+\beta\rho_0^{2/3}(r')\right]e^{-|\boldsymbol{r}-\boldsymbol{r}'|^2/\alpha_w^2}, \qquad (2)$$

where v and w are the depth parameters, β is the density-dependence parameter, and α_v and α_w are the range parameters for real and imaginary parts of the αN interaction, respectively.

The density distributions of the ground states of the target nuclei were taken from the results of the electron scattering measurements. The charge distributions of ^{12}C, ^{16}O, ^{24}Mg, ^{28}Si, and ^{40}Ca were parameterized in the form of the sum of Gaussian functions [41], while that of ^{20}Ne was in the form of the two-parameter Fermi model [42]. We calculated the point-proton distributions of the target nuclei by unfolding their charge distributions with the proton charge form factor [43,44]. The point-neutron distributions were assumed to be same with the point-proton distributions for these self-conjugate $A = 4n$ nuclei.

The parameters in Eq. (2) were determined to reproduce the cross sections of elastic scattering. We assumed the same range for real and imaginary parts of the interaction ($\alpha_v = \alpha_w$). The density-dependence parameter β was fixed at -1.9 or 0.0. The parameter value of $\beta = -1.9$ was proposed in Ref. [40], and widely used for the analysis of inelastic alpha scattering [2,4–10,13,20,25,28,29]. On the other hand, the parameter value of $\beta = 0.0$ means that the interaction is independent of the density of the target nucleus. For comparison between density-dependent and density-independent interactions, we determined two different sets of the interaction parameters with $\beta = -1.9$ and 0.0 for each nucleus. In this paper, the αN interactions with $\beta = 0.0$ are denoted by "DI" (density independent), whereas those with $\beta = -1.9$ are denoted by "DD" (density dependent).

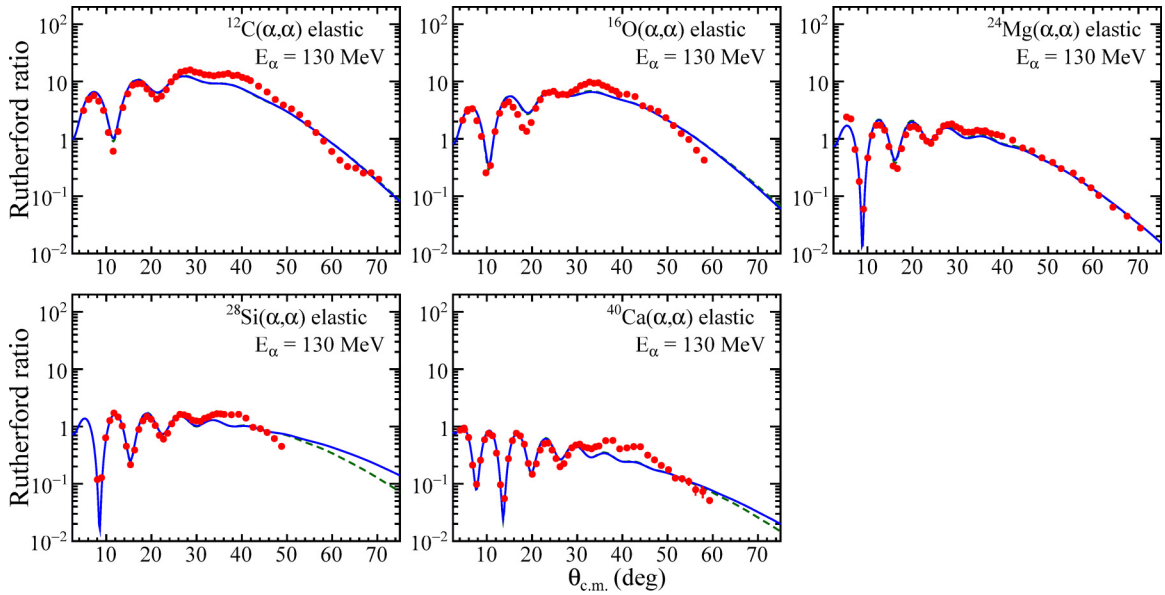

FIG. 5. Same as Fig. 5, but for ^{12}C, ^{16}O, ^{24}Mg, ^{28}Si, and ^{40}Ca at $E_\alpha = 130$ MeV.

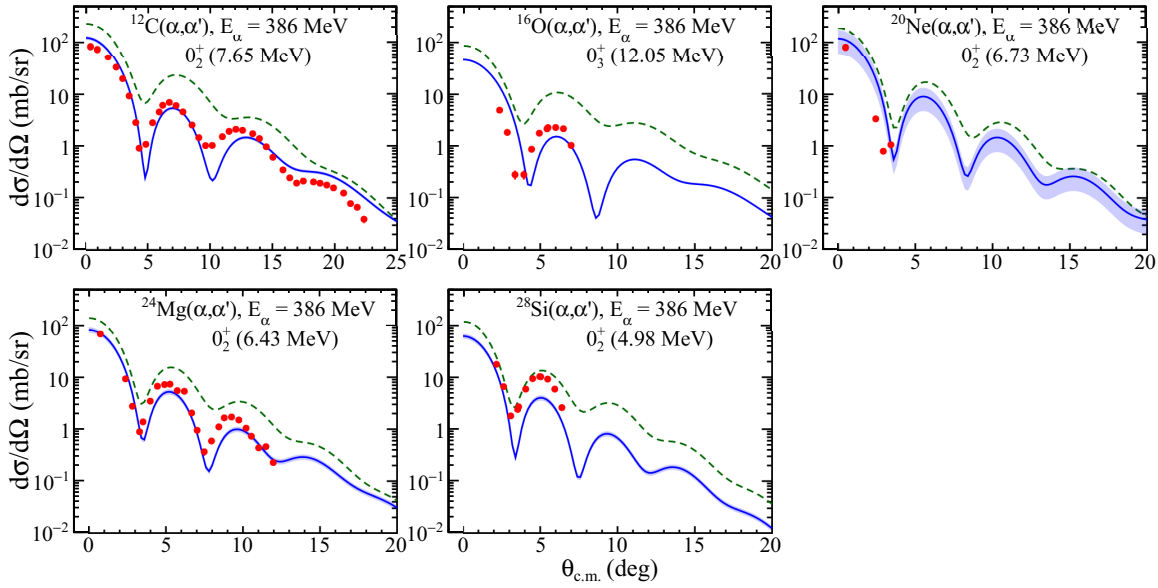

FIG. 6. Measured cross sections of the (α,α') reaction for the $\Delta L = 0$ transitions at $E_\alpha = 386$ MeV compared with the theoretical calculations. The solid circles with error bars show the measured cross sections. The solid lines with error bands and dashed lines are the theoretical calculations with the density-independent (DI) and density-dependent (DD) αN interactions, respectively. The error bands are shown for the theoretical calculations with DI interactions only. For details about the theoretical calculations, see Sec. III.

The calculated cross sections with the best-fit parameter values to the elastic scattering data at $E_\alpha = 386$ and 130 MeV are shown in Figs. 4 and 5, respectively. The cross sections calculated with the DI and DD interactions are almost the same.

As described in Sec. II, there are no available data of elastic α scattering off ^{28}Si and ^{40}Ca at $E_\alpha = 386$ MeV. Therefore, we could not determine the parameters of the interactions for these nuclei by fitting the cross sections of elastic α scattering. We fit the elastic α scattering data of ^{58}Ni, ^{90}Zr, ^{116}Sn, ^{144}Sm, and ^{208}Pb at $E_\alpha = 386$ MeV taken from Refs. [6] and determined the parameters for these nuclei as shown in Fig. 14. Although the parameters scatter for the lighter nuclei than ^{24}Mg, we could see the approximate linear relation between the parameters and $A^{1/3}$ for the heavier nuclei. We interpolate the parameters for the heavier nuclei as drawn by the solid lines in Fig. 14, and determined the parameters for ^{28}Si and ^{40}Ca. Although Fig. 14 shows the depth and range parameters of the DI interaction at $E_\alpha = 386$ MeV only, the same analysis could be done for the DD interaction.

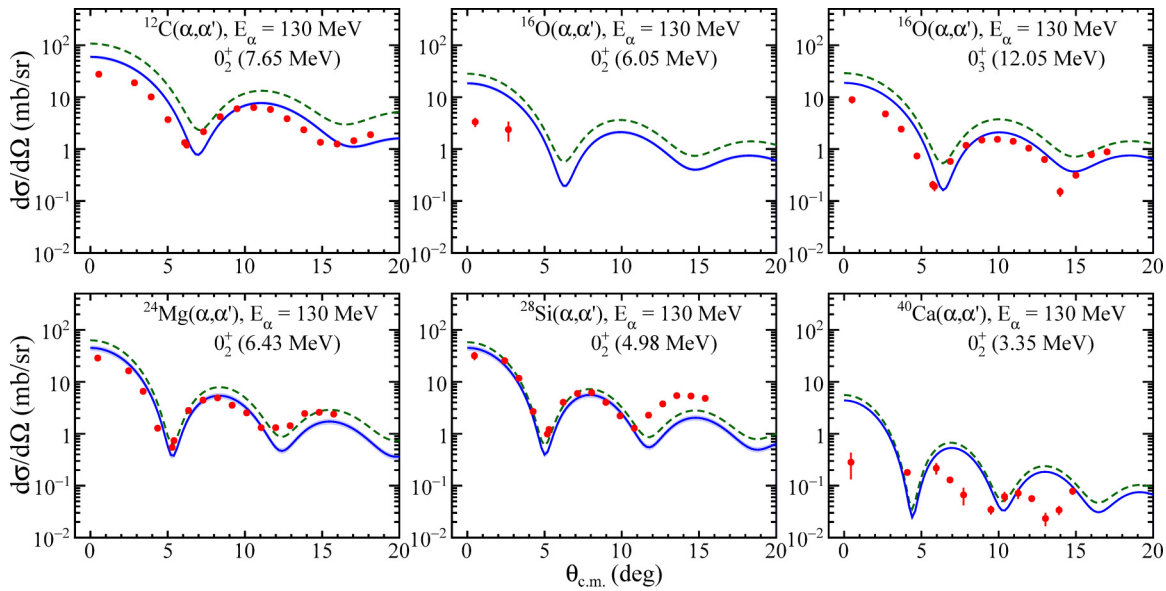

FIG. 7. Same as Fig. 6, but the cross sections for the $\Delta L = 0$ transitions at $E_\alpha = 130$ MeV.

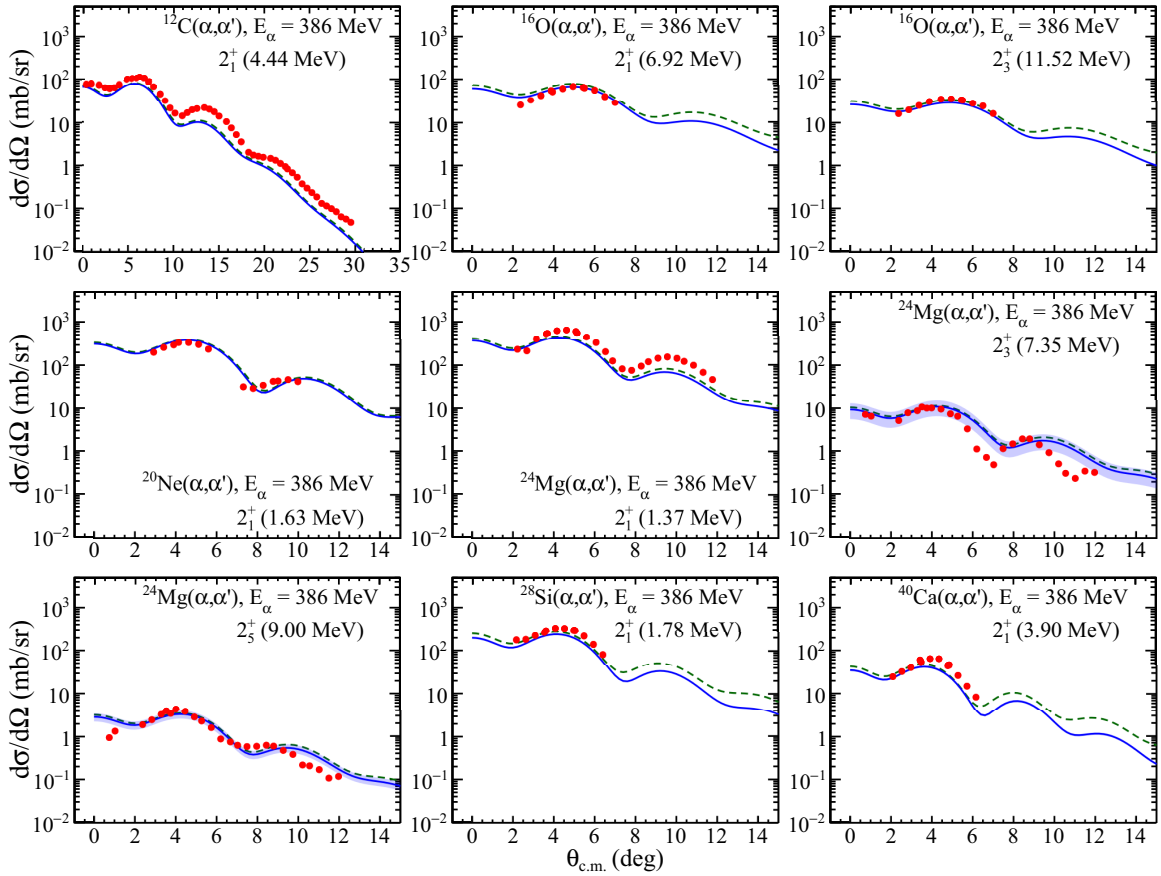

FIG. 8. Same as Fig. 6, but the cross sections for the $\Delta L = 2$ transitions at $E_\alpha = 386$ MeV.

B. Macroscopic transition potentials

We used the macroscopic charge transition densities for isoscalar transitions calculated from the standard macroscopic models [45,46]. The charge transition density $\tilde{\rho}^{(\lambda)}_{J_f,J_i}(r')$ for a transferred angular momentum λ with the initial-state spin J_i and the final-state spin J_f is given as follows:

$$\tilde{\rho}^{(0)}_{J_f,J_i}(r') = -\alpha_0\left(3 + r'\frac{d}{dr'}\right)\tilde{\rho}_0(r'), \quad (\lambda = 0) \tag{3}$$

$$\tilde{\rho}^{(1)}_{J_f,J_i}(r') = -\frac{\beta_1}{\sqrt{3}R}\left[3r'^2\frac{d}{dr'} + 10r - \frac{5}{3}\langle r'^2\rangle\frac{d}{dr'} + \epsilon\left(r\frac{d^2}{dr'^2} + 4\frac{d}{dr'}\right)\right]\tilde{\rho}_0(r'), \quad (\lambda = 1) \tag{4}$$

$$\tilde{\rho}^{(\lambda)}_{J_f,J_i}(r') = -\delta_\lambda\frac{d}{dr'}\tilde{\rho}_0(r'), \quad (\lambda \geqslant 2), \tag{5}$$

where α_0 is the deformation parameter and δ_λ is the deformation length. $\tilde{\rho}_0(r')$ is the ground-state charge density distribution. β_1, R, and $\langle r'^2\rangle$ are the collective coupling parameter for the isoscalar dipole resonance, the half-density radius of the Fermi charge distribution, and the root-mean-square radius of the ground-state charge distribution, respectively. The details about Eq. (4) are described in Ref. [46]. The values of α_0 and δ_λ were determined to reproduce the known electromagnetic transition strengths [24,36–38].

The $E1$ transition between isoscalar states is forbidden to the first order. The observed $E1$ transitions between the isoscalar states are competitive processes between isovector transitions allowed by the isospin symmetry breaking and higher-order isoscalar transitions as squeezing oscillation. Since these two types of $E1$ transitions have different transition densities, it is not easy to determine the value of β_1 from the known electromagnetic transition strengths $B(E1)$. Therefore, we determined β_1 to fit the first diffraction maximum of the cross sections by the DWBA calculation using the DI interaction.

Considering the density dependence of the interaction $u[|\boldsymbol{r} - \boldsymbol{r}'|, \rho_0(r')]$ to the lowest order, the transition potential $\delta U_\lambda(r)$ is obtained by folding the transition density $\rho^{(\lambda)}_{J_f,J_i}(r')$ with $u[|\boldsymbol{r} - \boldsymbol{r}'|, \rho_0(r')]$ as follows:

$$\delta U_\lambda(r) = \int dr' \rho^{(\lambda)}_{J_f,J_i}(r')\left[u[|\boldsymbol{r} - \boldsymbol{r}'|, \rho_0(r')] + \rho_0(r')\frac{\partial u[|\boldsymbol{r} - \boldsymbol{r}'|, \rho_0(r')]}{\partial \rho_0(r')}\right]. \tag{6}$$

The transition density $\rho^{(\lambda)}_{J_f,J_i}(r')$ is given by unfolding the charge transition density $\tilde{\rho}^{(\lambda)}_{J_f,J_i}(r')$ with the proton-charge form factor.

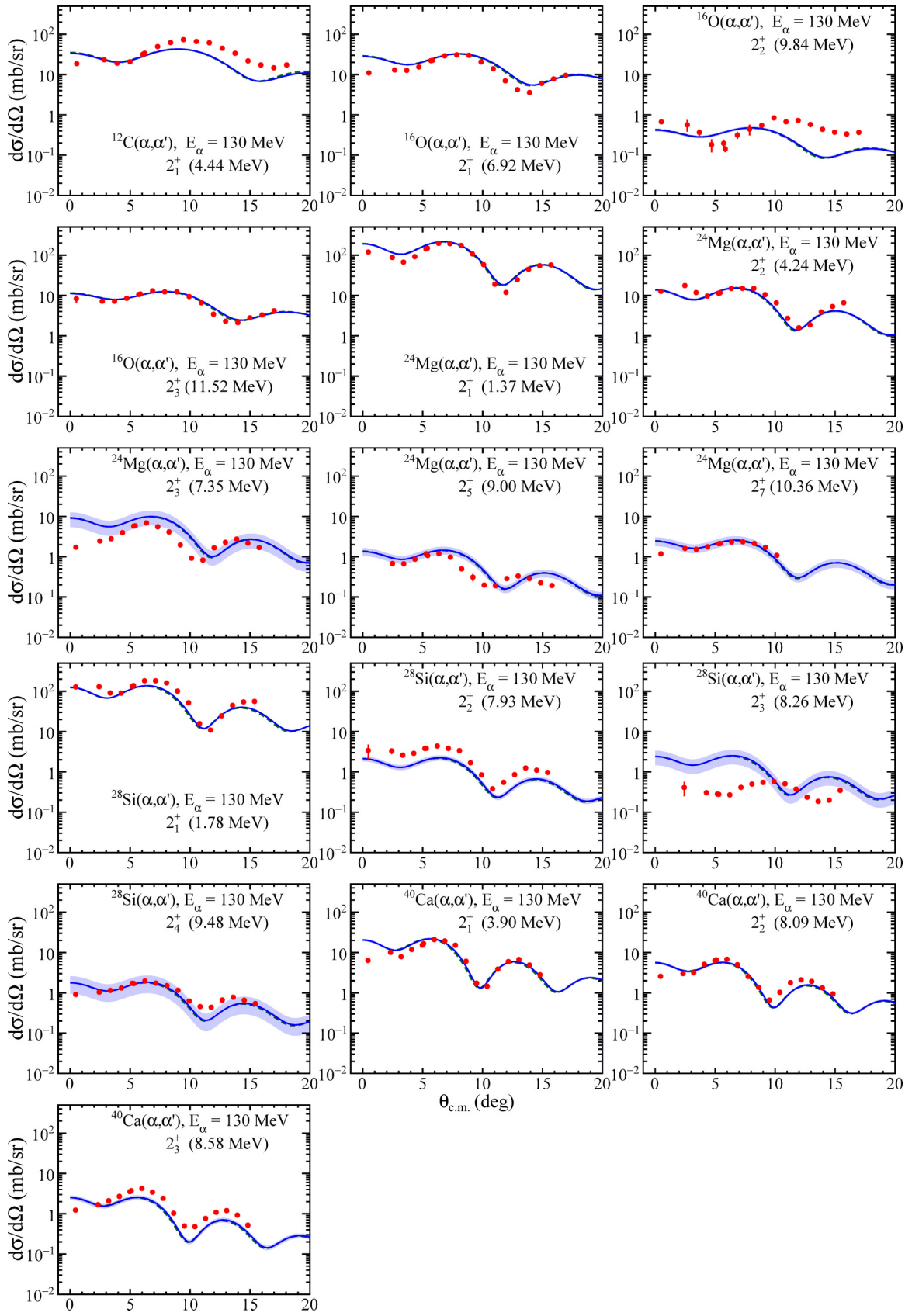

FIG. 9. Same as Fig. 6, but the cross sections for the $\Delta L = 2$ transitions at $E_\alpha = 130$ MeV.

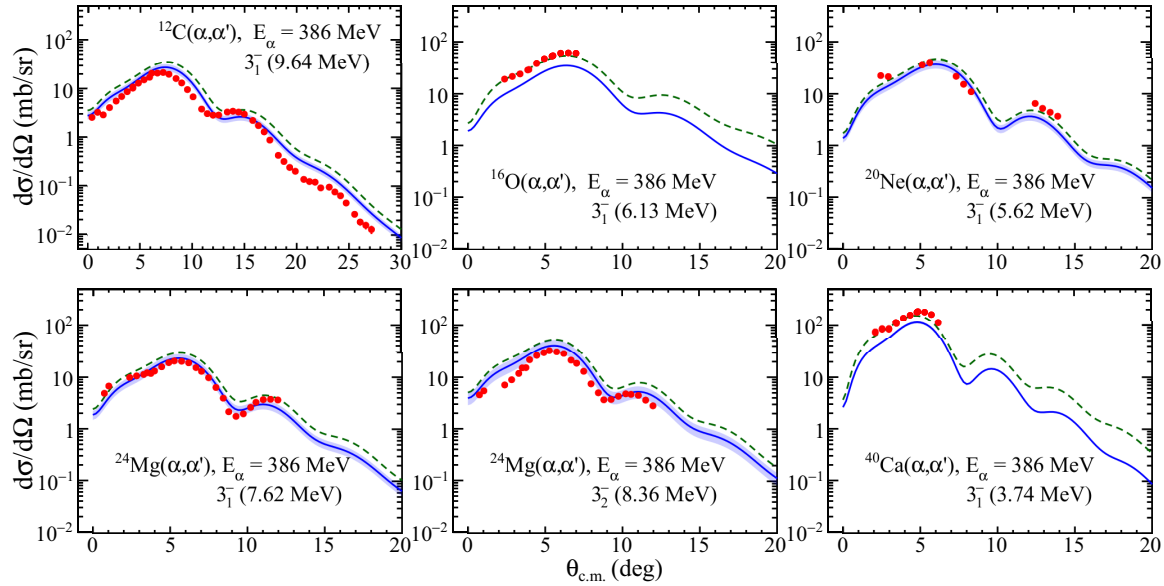

FIG. 10. Same as Fig. 6, but the cross sections for the $\Delta L = 3$ transitions at $E_\alpha = 386$ MeV.

It should be noted that there is no adjustable parameter in the present DWBA calculation because the αN interaction and transition densities are fixed by the elastic α scattering data and the known $B(E\lambda)$ values.

IV. DISCUSSION

A. Comparison between experimental data and DWBA calculations

Figures 6–13 show the comparison of the measured cross sections with the calculation using the DI and DD interactions.

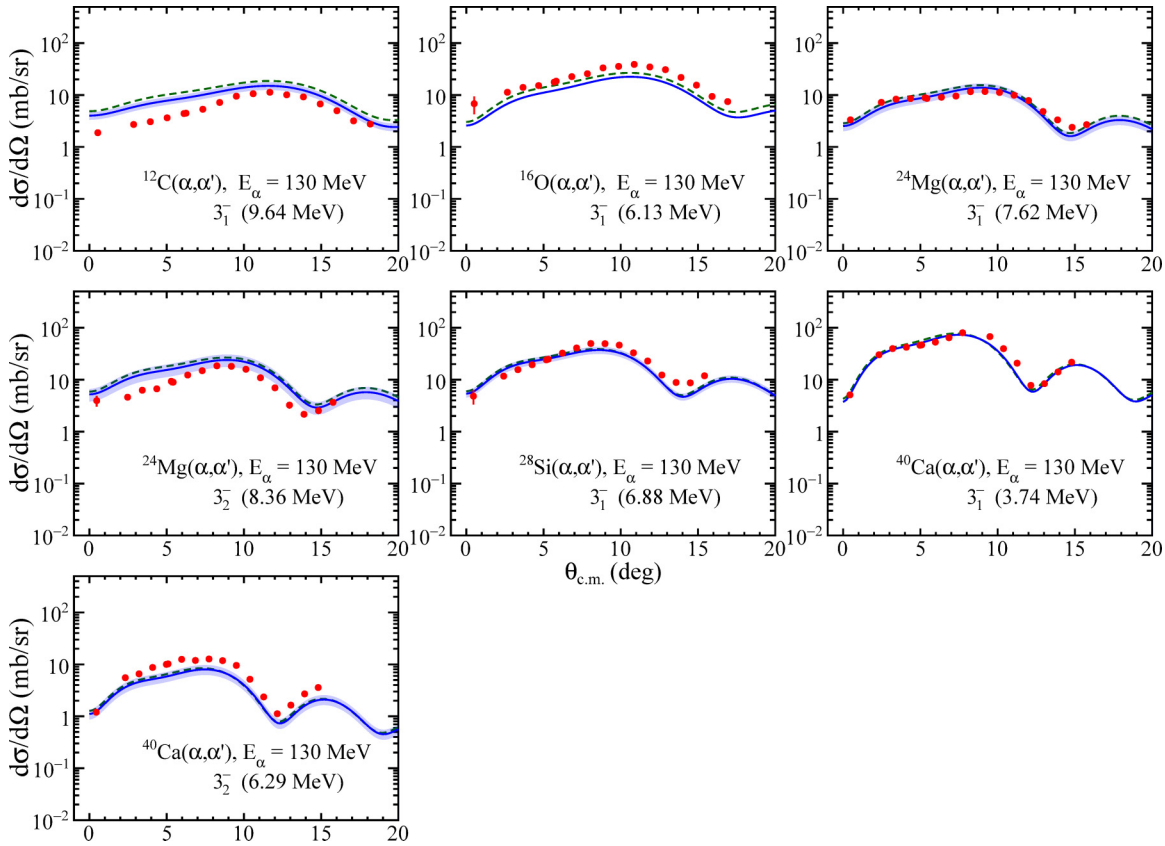

FIG. 11. Same as Fig. 6, but the cross sections for the $\Delta L = 3$ transitions at $E_\alpha = 130$ MeV.

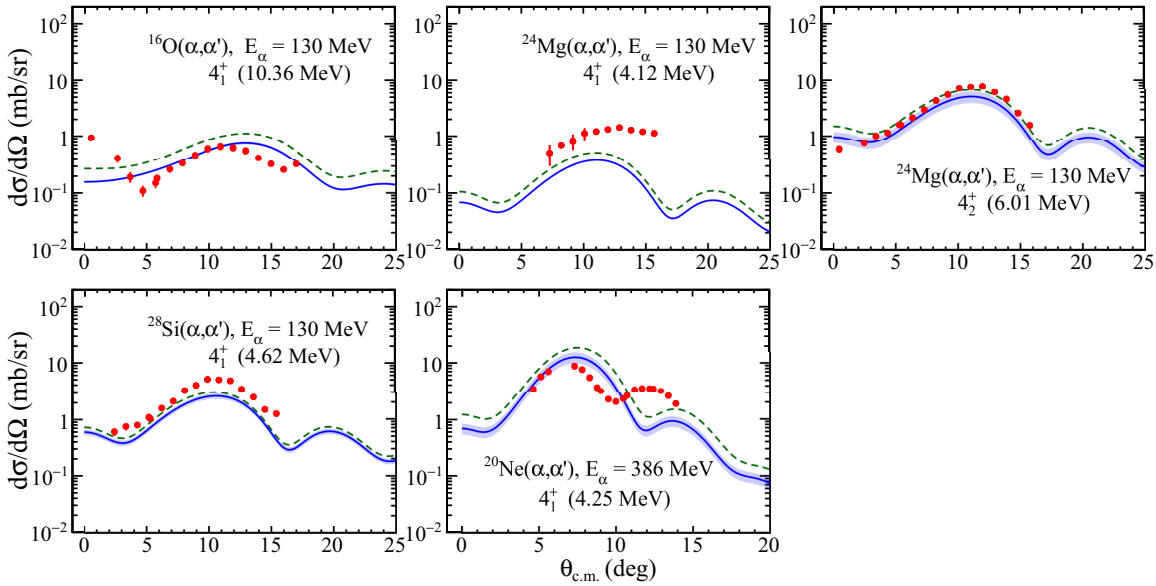

FIG. 12. Same as Fig. 6, but the cross sections for the $\Delta L = 4$ transitions at $E_\alpha = 130$ and 386 MeV.

Since the experimental cross sections were obtained for the angular bins with a width of 0.4°, the calculated cross sections at each angle are averaged over the angular range of ±0.2°.

As shown for the $\Delta L = 0$ transitions in Figs. 6 and 7, the calculated cross sections with the DD interactions are systematically larger than the measured cross sections. This discrepancy is consistent with the previous results in Refs. [27,31]. However, it should be noted that the DWBA calculations using the DD interaction overestimate the cross sections for not only the Hoyle state, but also most of the 0^+ states in ^{16}O, ^{20}Ne, ^{24}Mg, ^{28}Si, and ^{40}Ca. This result suggests that the missing monopole strength is not a special problem to the Hoyle state, but a universal problem for the $\Delta L = 0$ transitions. On the other hand, the calculated cross sections with the DI interactions are systematically smaller than those with the DD interactions, and are close to the measured cross sections. Especially, the calculation at $E_\alpha = 386$ MeV reasonably well reproduces the experimental data, and does not exhibit the puzzling situation about the missing monopole strength for the Hoyle state. The measured cross sections of the 0_2^+ states in ^{16}O and ^{40}Ca are much smaller than the calculations as seen in Fig. 7. The angular distributions of the measured cross sections for the 0_2^+ states are quite different from the calculations, but the reason for the discrepancy is still unclear. Both of these states are the first excited states in the double closed nuclei.

For the $\Delta L = 2$ transitions shown in Figs. 8 and 9, the DWBA calculations using the DI and DD interactions give almost the same results, and reasonably reproduce the angular distributions of the cross sections except for the several states. For the 2_2^+ state in ^{16}O and the 2_3^+ state in ^{28}Si, the calculated angular distributions of the cross sections are considerably different from the experimental data. The measured cross sections for these 2^+ states are smaller than 1 mb/sr. Since the direct couplings between the ground states and these states are weak, the multistep processes would be important to reproduce the cross sections for these states. For the 2_3^+ and 2_5^+ states in ^{24}Mg, the angular distributions of the measured cross sections slightly shift to forward angles compared with the DWBA calculations. This shift would be understandable if we assume that the radii of these states are larger than those of the usual states. In Refs. [47,48], it was theoretically shown that the angular distribution of inelastic cross sections for the $\Delta L = 0$ transition is not sensitive to the radial expansion of the excited

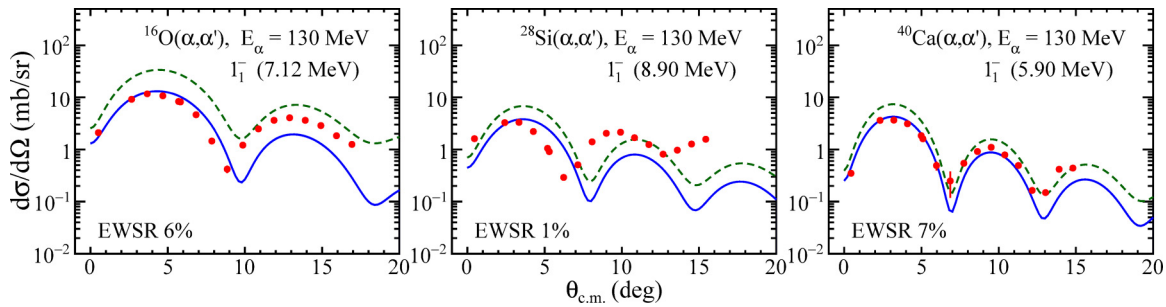

FIG. 13. Same as Fig. 6, but the cross sections for the $\Delta L = 1$ transitions at $E_\alpha = 130$ MeV. Note that the calculated cross sections are normalized to exhaust 6%, 1%, and 7% of the EWSR strengths of the isoscalar dipole transitions in ^{16}O, ^{28}Si, and ^{40}Ca, respectively.

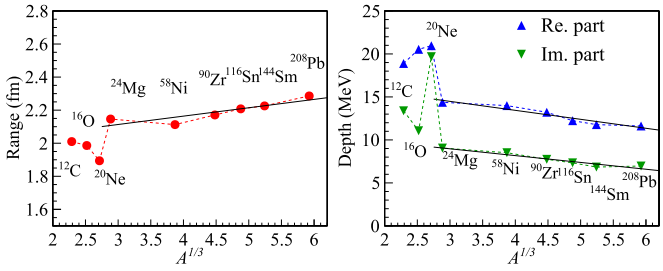

FIG. 14. Depth and range parameters of the phenomenological density-independent (DI) αN interaction at $E_\alpha = 386$ MeV as a function of $A^{1/3}$. The solid circles show the range parameters $\alpha_v = \alpha_w$, whereas the upward and downward triangles show the real and imaginary depth parameters v and w, respectively. The solid lines are the results of the linear fitting to the parameters at $A = 24$–208. The dotted lines connect each parameter points to guide the eyes.

states. However, the recent theoretical study suggests that the situation in the $\Delta L = 2$ transition is different from the $\Delta L = 0$ transition [49]. The shift of the angular distribution due to the radial expansion of the excited states is more visible in the $\Delta L = 2$ transition than in the $\Delta L = 0$ transition, and is more visible at lower reaction energies than at higher reaction energies. This is consistent with the present results that the shift in the angular distribution is more visible at $E_\alpha = 130$ MeV than at $E_\alpha = 386$ MeV. For the $\Delta L = 3$ and 4 transitions shown in Figs. 10–12, the differences between the calculations with the DI and DD interactions are small, although the DI interaction gives slightly small cross sections.

For the $\Delta L = 1$ transitions shown in Fig. 13, we can not directly compare the absolute values of the calculated cross sections with the experimental data since the known electromagnetic transition strengths $B(E1)$ can not be related to the collective coupling parameter of the transition density in Eq. (4). Therefore, the calculated cross sections are normalized to exhaust 6%, 1%, and 7% of the EWSR strengths of the isoscalar dipole transitions for ^{16}O, ^{28}Si, and ^{40}Ca, respectively. Although the diffraction pattern of the cross sections are reproduced well by the DWBA calculations using both the DI and DD interactions, the DI interactions give systematically smaller cross sections than the DD interactions as in the other multipole transitions.

The calculated cross sections for the (α,α') reactions at $E_\alpha = 386$ MeV are fitted to the experimental data by applying the normalization factor R. The isoscalar transition strengths $B(E\lambda; IS)$ determined by inelastic α scattering are related to the electromagnetic transition strength $B(E\lambda)$ as $B(E\lambda; IS) = 4B(E\lambda)/e^2$ assuming that the neutron transition density is same with the proton transition density. The normalization factor R is shown in Fig. 15 for the $\Delta L = 0, 2$, and 3 transitions. The R values for the DI interaction are systematically closer to the unity than those for the DD interaction, although the R values for the 0_2^+ states in ^{16}O, in ^{20}Ne, and in ^{28}Si significantly deviate from the unity.

The cross section for the 0_2^+ states in ^{20}Ne calculated with the DI interaction is consistent with the experimental data at 0° within the error due to the uncertainty from the electromagnetic transition strength. However, the disagreement between the

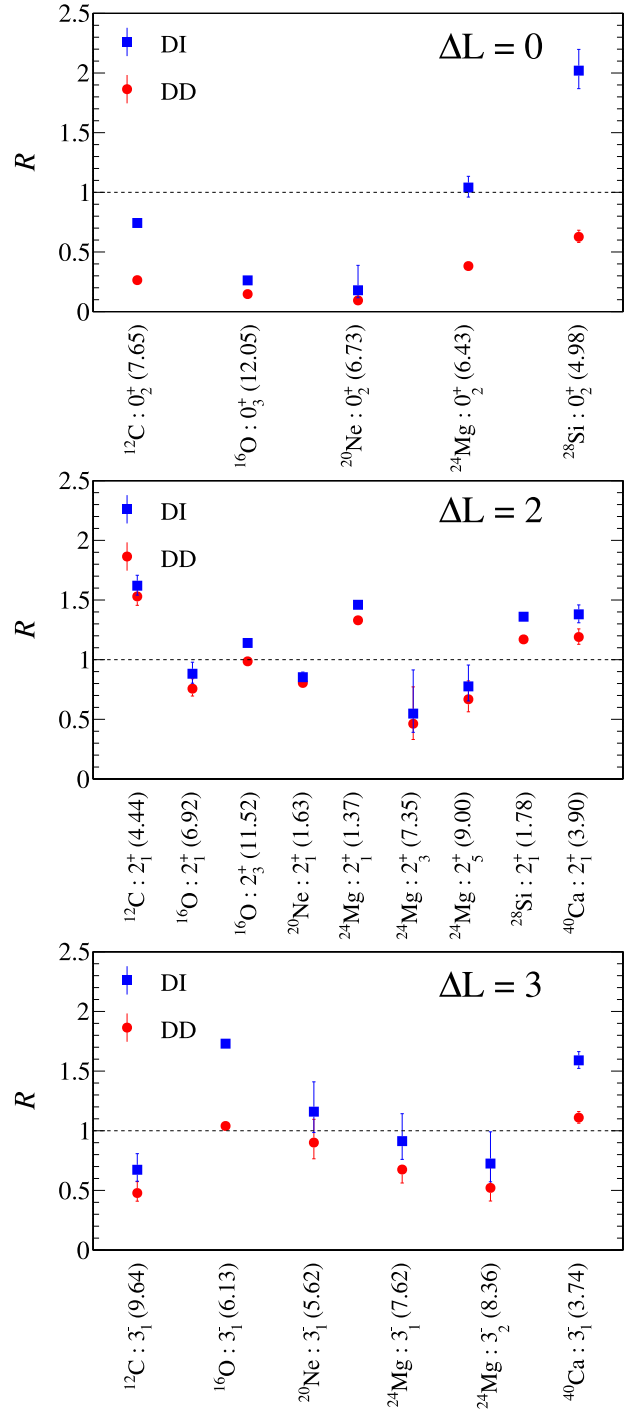

FIG. 15. Normalization factors for the calculated cross sections for the (α,α') reactions at $E_\alpha = 386$ MeV to fit the experimental data. The solid squares and circles are the normalization factors for the calculations with the DI and DD interactions. The errors come from the known electromagnetic transition transitions [23,24,36–38].

calculation and the experiment around the diffraction minimum causes the deviation of R from the unity.

The cross sections of the 0_3^+ state in ^{16}O and the 0_2^+ state in ^{28}Si were not measured at 0°. Since the cross sections near 0° are crucial for the reliable determination of the isoscalar

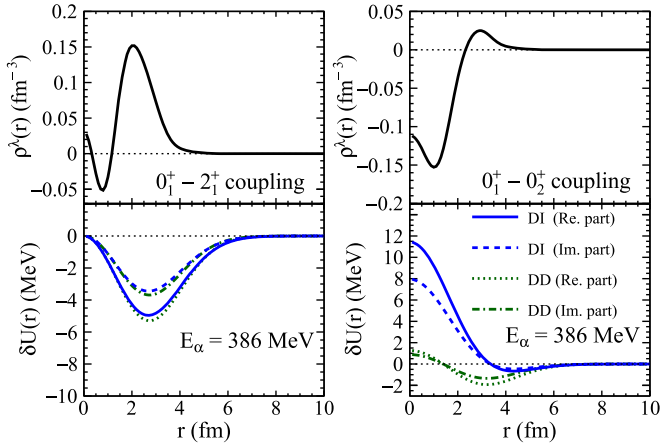

FIG. 16. Transition densities given by Eqs. (3) and (5), and the transition potentials with the phenomenological αN interaction. The top panels show the transition densities, and the bottom show the transition potentials for the 0_1^+–2_1^+ and 0_1^+–0_2^+ transitions in ^{12}C at $E_\alpha = 386$ MeV. The solid and dashed lines show the real and imaginary parts of the transition potentials with the DI interaction. The dotted and dot-dashed lines show the real and imaginary parts of the potentials with the DD interaction.

monopole transition strength, further measurements for these states should be done.

As discussed above, the DWBA calculation with the DI interaction gives a better description for inelastic α scattering than those with the DD interaction. Furthermore, the DI interaction at $E_\alpha = 386$ MeV is more applicable to fit the experimental data than that at $E_\alpha = 130$ MeV. This situations is naturally understood from the well-known fact that direct processes are dominant and the reaction mechanism becomes simple above $E \sim 100$ MeV/u.

B. Characteristics of the macroscopic transition densities and potentials

The transition densities and potentials in the present folding-model analyses should be examined in order to clarify the reason why the DI and DD interactions give the different results for the $\Delta L = 0$ transitions (see Figs. 6 and 7). Figure 16 shows the transition densities and potentials calculated based on the macroscopic model for the transitions between the ground and excited states in ^{12}C at $E_\alpha = 386$ MeV. The DI and DD interactions give similar potentials for the 2_1^+ state, whereas these two interactions give significantly different transition potentials for the 0_2^+ state. The transition density for the $\Delta L = 0$ transition has sizable values around the origin. Since the DD interaction is much weaker than the DI interaction around the origin due to the density effect, the DD transition potential for the $\Delta L = 0$ transition is much shallower than the DI transition potential in the inner region. On the other hand, the transition density for the $\Delta L = 2$ transition is almost zero at the origin. Therefore, the DI and DD transition potentials are almost same for the $\Delta L = 2$ transition.

Historically, the density dependence of the phenomenological αN interaction was introduced to obtain better description of elastic α scattering at backward angles [40]. Although the depth and range parameters used for the DI and DD interactions are determined to fit elastic α scattering, cross sections of elastic α scattering are sensitive to the nuclear wave functions at the surface only because of the strong absorption [50]. Since the interaction parameters are basically tuned at the surface where the nuclear density is relatively low, the DD interaction gives a good description for the $\Delta L = 2$ transition whose transition density enhances near the surface, but does not for the $\Delta L = 0$ transition in which the interior transition density gives a sizable contribution to the transition potential. The weak absorption by the DD transition potential for the $\Delta L = 0$ transitions causes the systematic overestimation of the cross sections and missing monopole strengths. It should be noted that the transition potential for the 0_1^+–0_2^+ transition from the recent full microscopic calculation using the realistic NN interaction [51] is similar to the DI transition potential for the $\Delta L = 0$ transition. This fact supports the conclusion given in Sec. IV A that the DI interaction is more suitable for the single-folding model calculations to describe the $\Delta L = 0$ transition than the DD interaction.

C. Uncertainty in the DWBA calculations

We introduced several approximations to the present DWBA analyses. (i) The macroscopic transition densities are used instead of the realistic microscopic transition densities. (ii) The distorting potentials for the exit channels are assumed to be the same with the entrance channels. (iii) The interactions are approximated by the Gaussian-type phenomenological αN interaction. (iv) The coupled-channel effects are ignored.

These approximations might cause errors in the present analyses. Uncertainties from these approximations are discussed in the following. Only the calculations with the DI interaction at $E_\alpha = 386$ MeV are shown because the situation does not essentially change even for the DD interaction or at $E_\alpha = 130$ MeV.

1. Transition densities

Reliable transition densities from the microscopic calculation are available for well-studied nuclei such as ^{12}C. However, such reliable transition densities are not available to analyze experimental data in most cases, because the experimental studies are generally done for lesser-examined states. Hence, the macroscopic model is widely used to analyze inelastic α scattering. The macroscopic transition densities for the 2_1^+, 0_2^+, and 3_1^- states given by Eqs. (3) and (5) are shown by the solid lines in the bottom panels of Fig. 17. In addition, the dashed lines represent the microscopic transition densities for the 0_1^+–2_1^+ and 0_1^+–0_2^+ transitions from the α-particle condensate wave functions (so-called THSR wave functions) [52,53] and the transition density for the 0_1^+–3_1^- transition from 3α RGM calculations [16]. The amplitudes of the microscopic transition densities are normalized to reproduce the known electromagnetic transition strengths [23,24,36,37]. The cross sections for the 2_1^+, 0_2^+, and 3_1^- states at $E_\alpha = 386$ MeV obtained from the DWBA calculations using the microscopic and macroscopic transition densities are compared in the top panels of Fig. 17. The solid lines are the same calculations

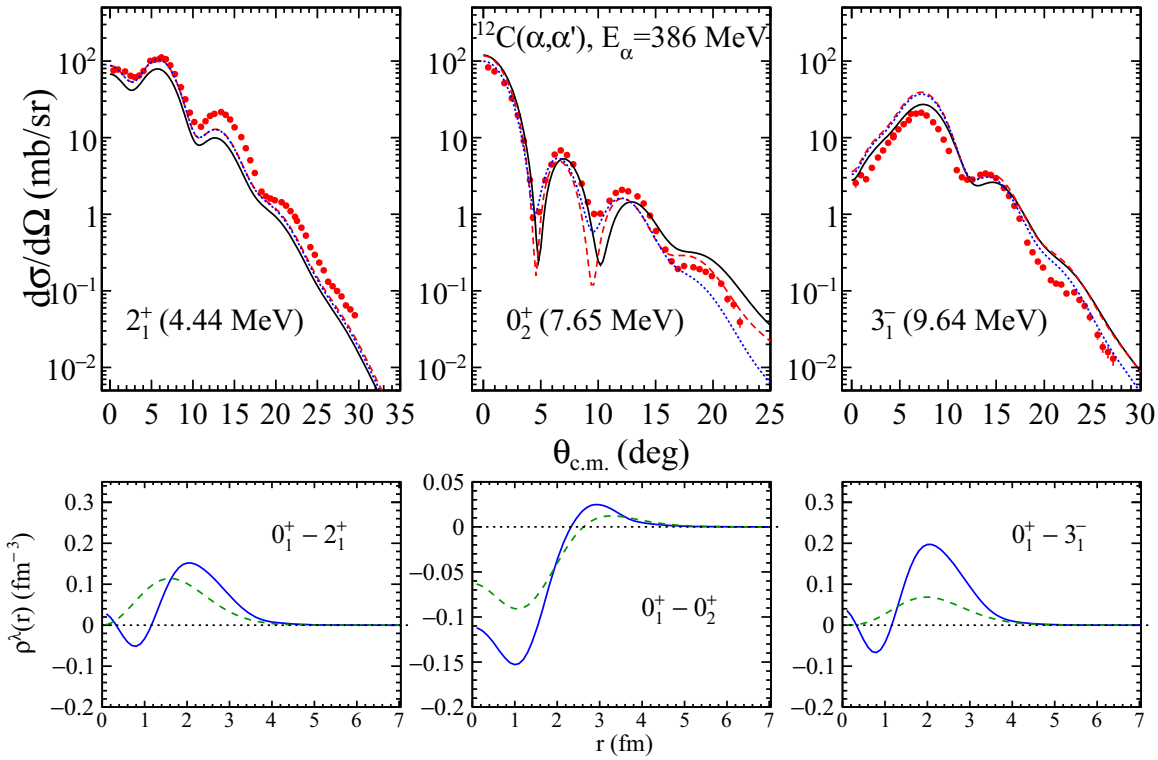

FIG. 17. Calculated cross sections and transition densities for the 2^+_1, 0^+_2, and 3^-_1 states in ^{12}C at $E_\alpha = 386$ MeV. The solid circles with error bars are the experimental data. The solid lines show the DWBA calculations using the DI interaction and macroscopic transition densities, which are same with the solid lines in Figs. 6, 8, and 10. The dashed lines show the DWBA calculations using the DI interaction and the microscopic transition densities from Refs. [16,52,53]. The dotted lines are the same DWBA calculations shown by the dashed lines except that the distorting potentials for the exit channels are calculated by folding the density distributions of the excited states with the DI interaction. The dashed and dotted lines are almost the same for the 2^+_1 and 3^-_1 states. In the bottom panels, the solid lines show the macroscopic transition densities given by unfolding the macroscopic charge transition densities [Eqs. (3) and (5)] with the proton charge form factor, whereas the dashed lines are the microscopic transition densities (see text).

as described in Sec. III using the DI interaction and the macroscopic transition densities. The dashed lines are the calculations using the DI interaction and the microscopic transition densities.

The differences between the solid and dashed lines in the top panels in Fig. 17 are very small for all of the 2^+_1, 0^+_2, and 3^-_1 states, although the macroscopic transition densities shown by the solid lines in the bottom panels are considerably different from the microscopic transition densities. These results show that the uncertainties due to differences in transition densities are negligibly small in the present DWBA calculation.

2. Distorting potentials

In order to examine uncertainties from the distorting potentials, we replace the distorting potentials for the exit channels with the diagonal potentials for the excited states. The diagonal optical-model potentials are calculated by folding the density distributions of the excited states from Refs. [16,52,53] with the DI interaction. The calculated cross sections are represented by the dotted lines in the top panels of Fig. 17. The cross sections for the 2^+_1 and 3^-_1 states do not change even if the distorting potentials are replaced. For the 0^+_2 state, on the other hand, the cross sections slightly change when the distorting potentials are replaced. This result is explained from the fact that the radius of the 0^+_2 state is much larger than that of the ground state [16,52,53] and thus, the distorting potential for the exit channel is very different from that for the entrance channel. However, the variation of the cross sections due to the distorting potential is acceptably small.

3. Phenomenological αN interaction

The present DWBA calculation using the single-folding potentials assumes the α particle is a point particle, and the phenomenological αN interaction is empirically determined to reproduce elastic α scattering. This interaction is really phenomenological, and hence it is not established on the realistic NN interaction. The present DWBA calculation should be compared with the calculation using the realistic NN interaction. In the following calculations, we used the diagonal potentials for the excited states as the distorting potential for the exit channels as performed in Sec. IV C 2.

For comparison, we carried out the DWBA calculation using the NN G-matrix interaction by the Melbourne group [54]. The transition potentials were calculated by doubly folding the projectile and target transition density distributions with the NN G-matrix interaction. The density distributions used with the NN G-matrix interaction are taken from the 3α RGM calculation [16], the same prescription as in Ref. [51]. The

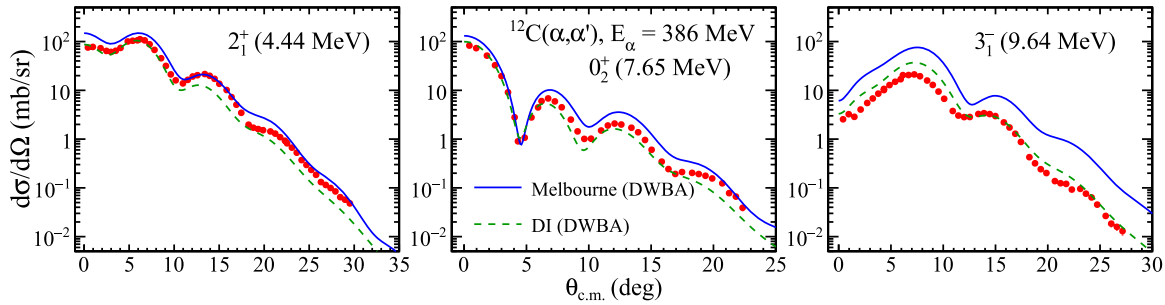

FIG. 18. Calculated cross sections of the inelastic α scattering at $E_\alpha = 386$ MeV exciting the 2_1^+, 0_2^+, and 3_1^- states in ^{12}C. The solid and dashed lines show the DWBA calculations with the Melbourne [54] and DI interactions, respectively. The solid circles with error bars are the experimental data.

calculated cross sections for the 2_1^+, 0_2^+, and 3_1^- states in ^{12}C with the Melbourne and DI interactions are shown by the solid and dashed lines in Fig. 18, respectively. The dashed lines are same as the dotted lines in the top panels of Fig. 17. Both the calculations reasonably reproduce the diffraction pattern of the measured cross sections. The cross sections with the DI interaction are systematically smaller than those with the Melbourne interaction, and are close to the experiment.

4. Coupled-channel effect

The coupled-channel (CC) effect is ignored in the present DWBA calculation, but it might not be negligible. Especially, it is pointed out that the coupling between the 0_2^+ and 2_2^+ states in ^{12}C is very strong [16,55]. The CC calculation for the inelastic α scattering exciting the 2_1^+, 0_2^+, and 3_1^- states in ^{12}C using the DI interaction at $E_\alpha = 386$ MeV was compared with the DWBA calculation in the top panels of Fig. 19. The distorting and transition potentials are calculated by using the wave functions from the 3α RGM calculation [16] for the 3_1^- state and the THSR wave functions [52,53] for the 0_1^+, 2_1^+, 0_2^+, 2_2^+, and 4_1^+ states.

The dotted lines show the CC calculation taking into account the coupled-channel effects between the six states (0_1^+, 2_1^+, 0_2^+, 3_1^-, 2_2^+, and 4_1^+), while the dashed lines show the CC calculation taking into account the coupled-channel effects between the five states except the 2_2^+ state. The solid lines show the DWBA calculation, which is the same as the dashed lines in Fig. 18. The CC effects for the 2_1^+ and 3_1^- states are negligibly small, and the DWBA and CC calculations give similar results except for the 0_2^+ state. The DWBA and five-state CC calculations give similar results even for the 0_2^+ state, but the six-state CC calculation gives a smaller cross section at forward angles than the other calculations. In addition, the diffraction pattern of the angular distribution in the six-state CC calculation slightly shifts to forward angles. This result reflects the fact that the coupling between the 0_2^+ and 2_2^+ states is strong.

The reduction of the cross section for the 0_2^+ state is essentially the same phenomenon as the enhanced absorption in the $\alpha + {}^{12}\mathrm{C}(0_2^+)$ channel proposed in Ref. [31]. It should be noted that the DWBA calculations are better to reproduce the experimental data than the six-state CC calculation. One possible explanation is that the coupling between the 0_2^+ and 2_2^+ states in the present CC calculation is too strong. The transition strength between the 0_2^+ and 2_2^+ states have never been measured, therefore the experimental study is strongly desired.

Recently, a full microscopic calculation of the inelastic α scattering from ^{12}C using the Melbourne NN G-matrix interaction was performed [51]. The CC calculations reported in Ref. [51] are shown in the bottom panels of Fig. 19. The dotted and dashed lines show the six-state and five-state CC calculations, respectively. On the other hand, the solid lines show the DWBA calculations, the same as the solid lines in Fig. 18. The situation is quite similar to the calculation with the DI interactions. The coupling to the 2_2^+ state is negligibly small for the 2_1^+ and 3_1^- states but not for the 0_2^+ state. The six-state CC calculation gives smaller cross sections of the 0_2^+ state than the five-state CC calculations at forward angles, and the diffraction pattern of the angular distribution in the six-state CC calculation slightly shifts to forward angles. The full microscopic CC calculation slightly underestimates the experimental cross sections for the 0_2^+ state at forward angles and overestimates at backward angles. The three-nucleon force possibly decreases the cross section at backward angles and improves the calculation as discussed in Ref. [51].

As discussed above, the CC effects are negligibly small in most cases of inelastic α scattering although the CC effects sometimes give sizable modification to cross sections. The DWBA calculation using the DI interaction at $E_\alpha = 386$ MeV reasonably reproduces the experimental results even for the 0_2^+ state in ^{12}C.

V. SUMMARY AND CONCLUSIONS

We systematically measured differential cross sections of inelastic α scattering off self-conjugate $A = 4n$ nuclei at two different incident energies $E_\alpha = 130$ and 386 MeV at RCNP, Osaka University. The measured cross sections were analyzed by the DWBA calculation with the single-folding potentials obtained by folding the macroscopic transition densities with the phenomenological αN interaction.

The DWBA calculation with the DI interaction reproduces the experimental data better than that with the DD interaction. The DWBA calculation with the DD interaction systematically overestimates the cross sections for $\Delta L = 0$ transitions. This result is consistent with the previous results [27,31], suggesting

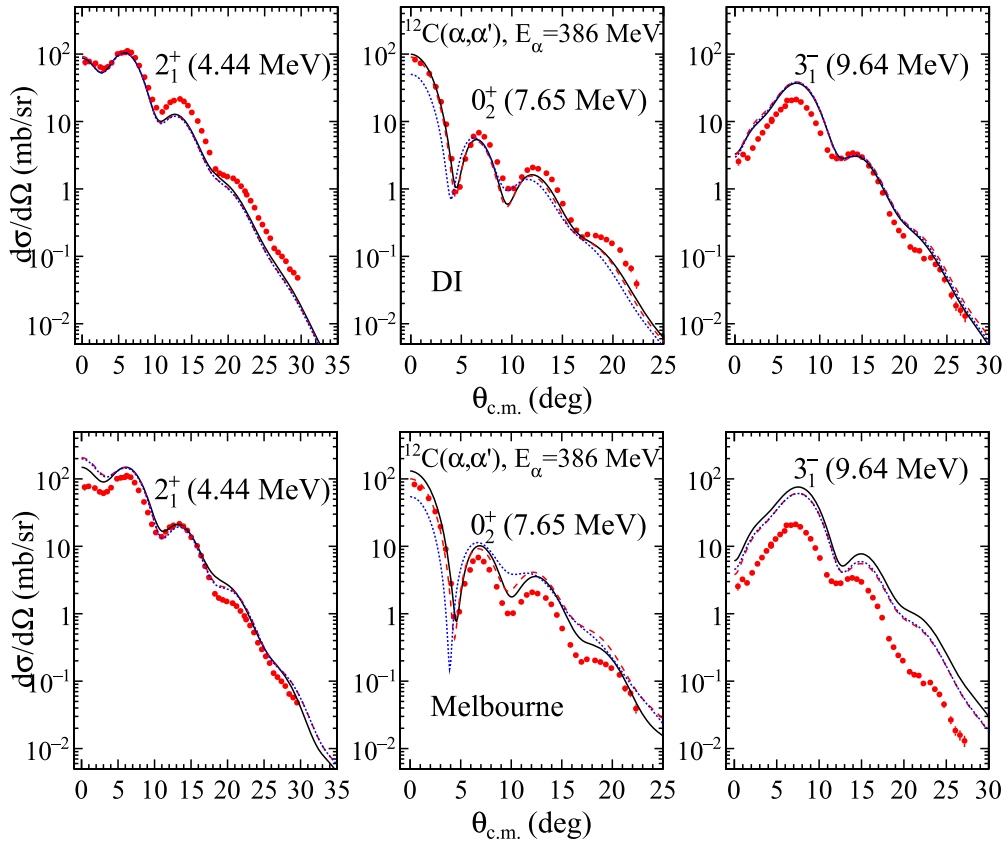

FIG. 19. Calculated cross sections of inelastic α scattering at $E_\alpha = 386$ MeV exciting the 2_1^+, 0_2^+, and 3_1^- states in ^{12}C. The top panels are the DWBA and CC calculations with the DI interaction, and the bottom panels are the calculations with the Melbourne interaction [51]. The solid lines show the DWBA calculation. The dotted and dashed lines respectively show the six-state and five-state CC calculations (see text). The dotted and dashed lines are almost the same for the 2_1^+ and 3_1^- states. The solid circles with error bars are the experimental data.

a puzzle of the missing monopole strength for exciting the 0_2^+ state in ^{12}C. However, we found that this discrepancy is not special to the 0_2^+ state in ^{12}C, but is universally observed in all of $\Delta L = 0$ transitions. The overestimation of the cross section by the DD interaction is due to the strong density dependence in the inner region of the target nucleus. The inadequate density dependence in the effective interaction is one reason for the puzzle of the missing monopole strength. On the other hand, the DWBA calculation using the DI interaction gives a reasonable description for the 0_2^+ state, and does not exhibit the problem of the missing monopole strength. The transition potential calculated with the DI interaction is actually similar to the double-folding transition potential obtained from the recent full microscopic calculation using the Melbourne G-matrix interaction constructed from the realistic NN interaction.

We also found that the DI interaction at $E_\alpha = 386$ MeV gives a better description than at $E_\alpha = 130$ MeV. It is naturally understood from the well-known fact that direct processes are dominant and the reaction mechanism becomes simple above $E \sim 100$ MeV/u. The DI interaction at $E_\alpha = 386$ MeV is the most suitable among the four interactions (DI or DD, $E_\alpha = 130$ or 386 MeV) to analyze the inelastic α scattering. The DWBA calculation using this interaction reasonably well describes all the transitions with $\Delta L = 0$–4.

Uncertainties in the present DWBA calculation were examined for ^{12}C. We found that the DWBA calculation is not sensitive to the details of the transition densities nor the distorting potentials. We compared the single-folding calculation using the DI interaction with the double-folding calculation using the Melbourne NN G-matrix interaction, and found the single-folding calculation gives reasonable description.

The CC effects are negligibly small for the 2_1^+ and 3_1^- states but not for the 0_2^+ state in ^{12}C. The 0_2^+ state is theoretically predicted to strongly couple to the 2_2^+ state. The cross section for the 0_2^+ state decreases at forward angles by taking into account the coupling with the 2_2^+ state. This reduction of the cross section for the 0_2^+ state is essentially the same phenomenon as the enhanced absorption in the $\alpha + {}^{12}\mathrm{C}(0_2^+)$ channel proposed in Ref. [31], and might be another reason for the puzzle of the missing monopole strength. However, the CC calculation underestimates the cross section, suggesting that the deduced monopole strength becomes larger than expected. One possible explanation is that the coupling between the 0_2^+

and 2_2^+ states in the present CC calculation is too strong. The experimental determination of the coupling strength between the 0_2^+ and 2_2^+ state is strongly desired.

Recently, a full microscopic CC calculation using the Melbourne G-matrix interaction was found to give a good description of the inelastic α scattering [51]. Although this microscopic CC calculation is established on the realistic NN interaction and is more sophisticated framework than the macroscopic DWBA calculation, such a calculation can be only carried out for the well-studied nuclei such as ^{12}C only. Most of experimental studies are done for unexplored states in various nuclei. The microscopic CC calculation cannot be applied for such states, but the macroscopic DWBA calculation is applicable. Therefore, we conclude that the macroscopic DWBA calculations using the DI interaction are reliably applicable to analyze inelastic α scattering at $E_\alpha \sim 100$ MeV/u.

ACKNOWLEDGMENTS

The authors acknowledge the RCNP cyclotron crews for providing a high-quality beam for background-free measurements at forward angles including 0°. The authors also thank Professor M. Ito, Professor Y. Kanada-Eny'o, Professor M. Kimura, and Professor M. Takashina for the valuable discussions about inelastic α scattering and the puzzle of the missing monopole strength.

This work was performed under the RCNP E253, E308, E369, and E402 programs. A part of experimental data, the cross sections of elastic α scattering at backward angles at $E_\alpha = 130$ MeV, was taken under the graduation research program by undergraduate students at Kyoto University (KADAIKENKYU P4). This work was partly supported by JSPS KAKENHI Grants No. JP15H02091 and No. JP23340068.

[1] D. H. Youngblood, Y.-W. Lui, and H. L. Clark, Phys. Rev. C **55**, 2811 (1997).
[2] D. H. Youngblood, Y.-W. Lui, and H. L. Clark, Phys. Rev. C **60**, 014304 (1999).
[3] D. H. Youngblood, H. L. Clark, and Y.-W. Lui, Phys. Rev. Lett. **82**, 691 (1999).
[4] M. Itoh, H. Sakaguchi, M. Uchida, T. Ishikawa, T. Kawabata, T. Murakami, H. Takeda, T. Taki, S. Terashima, N. Tsukahara, Y. Yasuda, M. Yosoi, U. Garg, M. Hedden, B. Kharraja, M. Koss, B. K. Nayak, S. Zhu, H. Fujimura, M. Fujiwara, K. Hara, H. P. Yoshida, H. Akimune, M. N. Harakeh, and M. Volkerts, Phys. Lett. B **549**, 58 (2002).
[5] M. Itoh, H. Sakaguchi, M. Uchida, T. Ishikawa, T. Kawabata, T. Murakami, H. Takeda, T. Taki, S. Terashima, N. Tsukahara, Y. Yasuda, M. Yosoi, U. Garg, M. Hedden, B. Kharraja, M. Koss, B. K. Nayak, S. Zhu, H. Fujimura, M. Fujiwara, K. Hara, H. P. Yoshida, H. Akimune, M. N. Harakeh, and M. Volkerts, Phys. Rev. C **68**, 064602 (2003).
[6] M. Uchida, H. Sakaguchi, M. Itoh, M. Yosoi, T. Kawabata, Y. Yasuda, H. Takeda, T. Murakami, S. Terashima, S. Kishi, U. Garg, P. Boutachkov, M. Hedden, B. Kharraja, M. Koss, B. K. Nayak, S. Zhu, M. Fujiwara, H. Fujimura, H. P. Yoshida, K. Hara, H. Akimune, and M. N. Harakeh, Phys. Rev. C **69**, 051301 (2004); M. Uchida, Ph.D. thesis, Kyoto University, 2003.
[7] M. Itoh, S. Kishi, H. Sakaguchi, H. Akimune, M. Fujiwara, U. Garg, K. Hara, H. Hashimoto, J. Hoffman, T. Kawabata, K. Kawase, T. Murakami, K. Nakanishi, B. K. Nayak, S. Terashima, M. Uchida, Y. Yasuda, and M. Yosoi, Phys. Rev. C **88**, 064313 (2013).
[8] T. Li, U. Garg, Y. Liu, R. Marks, B. K. Nayak, P. V. Madhusudhana Rao, M. Fujiwara, H. Hashimoto, K. Kawase, K. Nakanishi, S. Okumura, M. Yosoi, M. Itoh, M. Ichikawa, R. Matsuo, T. Terazono, M. Uchida, T. Kawabata, H. Akimune, Y. Iwao, T. Murakami, H. Sakaguchi, S. Terashima, Y. Yasuda, J. Zenihiro, and M. N. Harakeh, Phys. Rev. Lett. **99**, 162503 (2007).
[9] Y. K. Gupta, U. Garg, J. Hoffman, J. Matta, P. V. Madhusudhana Rao, D. Patel, T. Peach, K. Yoshida, M. Itoh, M. Fujiwara, K. Hara, H. Hashimoto, K. Nakanishi, M. Yosoi, H. Sakaguchi, S. Terashima, S. Kishi, T. Murakami, M. Uchida, Y. Yasuda, H. Akimune, T. Kawabata, and M. N. Harakeh, Phys. Rev. C **93**, 044324 (2016).
[10] T. Peach, U. Garg, Y. K. Gupta, J. Hoffman, J. T. Matta, D. Patel, P. V. Madhusudhana Rao, K. Yoshida, M. Itoh, M. Fujiwara, K. Hara, H. Hashimoto, K. Nakanishi, M. Yosoi, H. Sakaguchi, S. Terashima, S. Kishi, T. Murakami, M. Uchida, Y. Yasuda, H. Akimune, T. Kawabata, M. N. Harakeh, and G. Colò, Phys. Rev. C **93**, 064325 (2016).
[11] S. Bagchi, J. Gibelin, M. N. Harakeh, N. Kalantar-Nayestanaki, N. L. Achouri, H. Akimune, B. Bastin, K. Boretzky, H. Bouzomita, M. Caamaño, L. Càceres, S. Damoy, F. Delaunay, B. Fernández-Domínguez, M. Fujiwara, U. Garg, G. F. Grinyer, O. Kamalou, E. Khan, A. Krasznahorkay, G. Lhoutellier, J. F. Libin, S. Lukyanov, K. Mazurek, M. A. Najafi, J. Pancin, Y. Penionzhkevich, L. Perrot, R. Raabe, C. Rigollet, T. Roger, S. Sambi, H. Savajols, M. Senoville, C. Stodel, L. Suen, J. C. Thomas, M. Vandebrouck, and J. Van de Walle, Phys. Lett. B **751**, 371 (2015).
[12] M. Vandebrouck, J. Gibelin, E. Khan, N. L. Achouri, H. Baba, D. Beaumel, Y. Blumenfeld, M. Caamaño, L. Càceres, G. Colò, F. Delaunay, B. Fernandez-Dominguez, U. Garg, G. F. Grinyer, M. N. Harakeh, N. Kalantar-Nayestanaki, N. Keeley, W. Mittig, J. Pancin, R. Raabe, T. Roger, P. Roussel-Chomaz, H. Savajols, O. Sorlin, C. Stodel, D. Suzuki, and J. C. Thomas, Phys. Rev. C **92**, 024316 (2015).
[13] M. Itoh, H. Akimune, M. Fujiwara, U. Garg, N. Hashimoto, T. Kawabata, K. Kawase, S. Kishi, T. Murakami, K. Nakanishi, Y. Nakatsugawa, B. K. Nayak, S. Okumura, H. Sakaguchi, H. Takeda, S. Terashima, M. Uchida, Y. Yasuda, M. Yosoi, and J. Zenihiro, Phys. Rev. C **84**, 054308 (2011).
[14] H. Morinaga, Phys. Rev. **101**, 254 (1956).
[15] H. Morinaga, Phys. Lett. **21**, 78 (1966).
[16] M. Kamimura, Nucl. Phys. A **351**, 456 (1981).
[17] R. De Leo, G. D'Erasmo, A. Pantaleo, M. N. Harakeh, E. Cereda, S. Micheletti, and M. Pignanelli, Phys. Rev. C **28**, 1443 (1983).
[18] H. O. U. Fynbo, C. A. Diget, U. C. Bergmann, M. J. G. Borge, J. Cederkäll, P. Dendooven, L. M. Fraile, S. Franchoo, V. N. Fedosseev, B. R. Fulton, W. Huang, J. Huikari, H. B. Jeppesen,

A. S. Jokinen, P. Jones, B. Jonson, U. Köster, K. Langanke, M. Meister, T. Nilsson, G. Nyman, Y. Prezado, K. Riisager, S. Rinta-Antila, O. Tengblad, M. Turrion, Y. Wang, L. Weissman, K. Wilhelmsen, and J. Äystö, Nature (London) **433**, 136 (2005).

[19] M. Freer, H. Fujita, Z. Buthelezi, J. Carter, R. W. Fearick, S. V. Förtsch, R. Neveling, S. M. Perez, P. Papka, F. D. Smit, J. A. Swartz, and I. Usman, Phys. Rev. C **80**, 041303 (2009).

[20] T. Kawabata, H. Akimune, H. Fujita, Y. Fujita, M. Fujiwara, K. Hara, K. Hatanaka, M. Itoh, Y. Kanada-En'yo, S. Kishi, K. Nakanishi, H. Sakaguchi, Y. Shimbara, A. Tamii, S. Terashima, M. Uchida, T. Wakasa, Y. Yasuda, H. Yoshida, and M. Yosoi, Phys. Lett. B **646**, 6 (2007).

[21] B. F. Bayman and A. Bohr, Nucl. Phys. **9**, 596 (1958).

[22] T. Yamada, Y. Funaki, H. Horiuchi, K. Ikeda, and A. Tohsaki, Prog. Theor. Phys. **120**, 1139 (2008).

[23] M. Chernykh, H. Feldmeier, T. Neff, P. von Neumann-Cosel, and A. Richter, Phys. Rev. Lett. **105**, 022501 (2010).

[24] P. M. Endt, At. Data Nucl. Data Tables **55**, 171 (1993).

[25] T. Kawabata, T. Adachi, M. Fujiwara, K. Hatanaka, Y. Ishiguro, M. Itoh, Y. Maeda, H. Matsubara, H. Miyasako, Y. Nozawa, T. Saito, S. Sakaguchi, Y. Sasamoto, Y. Shimizu, T. Takahashi, A. Tamii, S. Terashima, H. Tokieda, N. Tomida, T. Uesaka, M. Uchida, Y. Yasuda, N. Yokota, H. P. Yoshida, and J. Zenihiro, J. Phys. Conf. Ser. **321**, 012012 (2011).

[26] Y. Chiba and M. Kimura, Phys. Rev. C **91**, 061302 (2015).

[27] B. John, Y. Tokimoto, Y.-W. Lui, H. L. Clark, X. Chen, and D. H. Youngblood, Phys. Rev. C **68**, 014305 (2003).

[28] Y. Sasamoto, T. Kawabata, T. Uesaka, K. Suda, Y. Maeda, S. Sakaguchi, K. Itoh, K. Hatanaka, M. Fujiwara, A. Tamii, Y. Shimizu, K. Nakanishi, K. Kawase, H. Hashimoto, Y. Tameshige, H. Matsubara, M. Itoh, H. P. Yoshida, and M. Uchida, Mod. Phys. Lett. A **21**, 2393 (2006).

[29] T. Wakasa, E. Ihara, K. Fujita, Y. Funaki, K. Hatanaka, H. Horiuchi, M. Itoh, J. Kamiya, G. Röpke, H. Sakaguchi, N. Sakamoto, Y. Sakemi, P. Schuck, Y. Shimizu, M. Takashina, S. Terashima, A. Tohsaki, M. Uchida, H. P. Yoshida, and M. Yosoi, Phys. Lett. B **653**, 173 (2007).

[30] P. Strehl, Z. Phys **234**, 416 (1970).

[31] D. T. Khoa and D. C. Cuong, Phys. Lett. B **660**, 331 (2007).

[32] T. Kawabata, H. Akimune, H. Fujimura, H. Fujita, Y. Fujita, M. Fujiwara, K. Hara, K. Hatanaka, K. Hosono, T. Ishikawa, M. Itoh, J. Kamiya, M. Nakamura, T. Noro, E. Obayashi, H. Sakaguchi, Y. Shimbara, H. Takeda, T. Taki, A. Tamii, H. Toyokawa, N. Tsukahara, M. Uchida, H. Ueno, T. Wakasa, K. Yamasaki, Y. Yasuda, H. P. Yoshida, and M. Yosoi, Nucl. Instrum. Meth. A **459**, 171 (2001).

[33] H. Matsubara, A. Tamii, Y. Shimizu, K. Suda, Y. Tameshige, and J. Zenihiro, Nucl. Instrum. Meth. A **678**, 122 (2012).

[34] M. Fujiwara, H. Akimune, I. Daito, H. Fujimura, Y. Fujita, K. Hatanaka, H. Ikegami, I. Katayama, K. Nagayama, N. Matsuoka, S. Morinobu, T. Noro, M. Yoshimura, H. Sakaguchi, Y. Sakemi, A. Tamii, and M. Yosoi, Nucl. Instrum. Meth. A **422**, 484 (1999).

[35] A. Tamii, Y. Fujita, H. Matsubara, T. Adachi, J. Carter, M. Dozono, H. Fujita, K. Fujita, H. Hashimoto, K. Hatanaka, T. Itahashi, M. Itoh, T. Kawabata, K. Nakanishi, S. Ninomiya, A. B. Perez-Cerdan, L. Popescu, B. Rubio, T. Saito, H. Sakaguchi, Y. Sakemi, Y. Sasamoto, Y. Shimbara, Y. Shimizu, F. D. Smit, Y. Tameshige, M. Yosoi, and J. Zenhiro, Nucl. Instrm. Methods Phys. Res., Sect. A **605**, 326 (2009).

[36] P. M. Endt, At. Data Nucl. Data Tables **23**, 3 (1979).

[37] P. M. Endt, Nucl. Phys. A **521**, 1 (1990).

[38] D. R. Tilley, C. M. Cheves, J. H. Kelley, S. Raman, and H. R. Weller, Nucl. Phys. A **636**, 249 (1998).

[39] J. Raynal, "Computer Program : ECIS-95" (1995), old version of ECIS-12 NEA-0850/19.

[40] G. R. Satchler and D. T. Khoa, Phys. Rev. C **55**, 285 (1997).

[41] H. De Vries, C. W. De Jager, and C. De Vries, At. Data Nucl. Data Tables **36**, 495 (1987).

[42] E. A. Knight, R. P. Singhal, R. G. Arthur, and M. W. S. Macauley, J. Phys. G : Nucl. Phys. **7**, 1115 (1981).

[43] J. J. Kelly, Phys. Rev. C **70**, 068202 (2004).

[44] S. Terashima, Ph.D. thesis, Kyoto University, 2008; S. Terashima, H. Sakaguchi, H. Takeda, T. Ishikawa, M. Itoh, T. Kawabata, T. Murakami, M. Uchida, Y. Yasuda, M. Yosoi, J. Zenihiro, H. P. Yoshida, T. Noro, T. Ishida, S. Asaji, and T. Yonemura, Phys. Rev. C **77**, 024317 (2008)

[45] G. R. Satchler, Nucl. Phys. A **472**, 215 (1987).

[46] M. N. Harakeh and A. E. L. Dieperink, Phys. Rev. C **23**, 2329 (1981).

[47] M. Takashina and Y. Sakuragi, Phys. Rev. C **74**, 054606 (2006).

[48] M. Takashina, Phys. Rev. C **78**, 014602 (2008).

[49] M. Tomita, M. Iwasaki, R. Otani, and M. Ito, in Proceedings of The 26th International Nuclear Physics Conference, PoS (**INPC2016**), 210 (2016).

[50] B. Bonin, N. Alamanos, B. Berthier, G. Bruge, H. Faraggi, J. C. Lugol, W. Mittig, L. Papineau, A. I. Yavin, J. Arvieux, L. Farvacque, M. Buenerd, and W. Bauhoff, Nucl. Phys. A **445**, 381 (1985).

[51] K. Minomo and K. Ogata, Phys. Rev. C **93**, 051601 (2016).

[52] Y. Funaki, A. Tohsaki, H. Horiuchi, P. Schuck, and G. Röpke, Eur. Phys. J. A **24**, 321 (2005).

[53] Y. Funaki, A. Tohsaki, H. Horiuchi, P. Schuck, and G. Röpke, Eur. Phys. J. A **28**, 259 (2006).

[54] K. Amos, P. J. Dortmans, H. V. von Geramb, S. Karataglidis, and J. Raynal, *in Advanced Nucler Physics*, edited by J. W. Negele and E. Vogt, Vol. 25 (Plenum, New York, 2000). p. 275.

[55] E. Uegaki, S. Okabe, Y. Abe, and H. Tanaka, Prog. Theor. Phys. **57**, 1262 (1977).